Pathogen-specific antimicrobials engineered *de novo* through membrane-protein biomimicry

Andrew W. Simonson[1], **Agustey S. Mongia**[1], **Matthew R. Aronson**[1], **John N. Alumasa**[2], **Dennis C. Chan**[1,3,4], **Atip Lawanprasert**[1], **Michael D. Howe**[5], **Adam Bolotsky**[6,7], **Tapas K. Mal**[8,9], **Christy George**[8,9], **Aida Ebrahimi**[1,6,7,10], **Anthony D. Baughn**[5], **Elizabeth A. Proctor**[1,3,4,11], **Kenneth C. Keiler**[2,12], **Scott H. Medina**[1,12,*]

[1]Department of Biomedical Engineering, Penn State University, University Park, PA, USA, 16801

[2]Department of Biochemistry and Molecular Biology, Penn State University, University Park, PA, USA, 16801

[3]Departments of Neurosurgery and Pharmacology, Penn State College of Medicine, Hershey, PA, USA, 17033

[4]Center for Neural Engineering, Penn State University, University Park, PA, USA, 16801

[5]Department of Microbiology and Immunology, University of Minnesota, Minneapolis, MN, USA, 55455

[6]Department of Materials Science and Engineering, Penn State University, University Park, PA, USA, 16801

[7]Materials Research Institute, Penn State University, University Park, PA, USA, 16801

[8]NMR Facility, Penn State University, University Park, PA, USA, 16801

[9]Department of Chemistry, Penn State University, University Park, PA, USA, 16801

[10]Department of Electrical Engineering, Penn State University, University Park, PA, USA, 16801

[11]Department of Engineering Science & Mechanics, Penn State University, University Park, PA, USA, 16801

[*]**Correspondence and requests for materials** should be addressed to S.H.M., shm126@psu.edu.

Author contributions

A.W.S. and S.H.M. conceived the hypothesis, designed the experiments, and wrote the manuscript. A.W.S., A.S.M., M.R.A., J.A., D.C.C., A.L., M.D.H., A.B., T.K.M., C.G., A.E., A.D.B., E.A.P. and K.C.K designed and performed the experiments, analyzed the results and contributed to writing of the manuscript.

Code availability

The parallelized Discrete Molecular Dynamics simulation engine (πDMD, v1.0) with Medusa all-atom force field is available from Molecules In Action, LLC (moleculesinaction.com). The software is available for free to academic users.

Competing interests

The authors declare no competing interests.

Additional information

Supplementary information is available for this paper at https://doi.org/10.1038/s41551-01X-XXXX-X.

Peer review information *Nature Biomedical Engineering* thanks Stephan Sieber and the other, anonymous, reviewers for their contribution to the peer review of this work.

[12]Huck Institutes of the Life Sciences, Penn State University, University Park, PA, USA, 16801

Abstract

Precision antimicrobials aim to kill pathogens without damaging commensal bacteria in the host, and thus to cure disease without antibiotic-associated dysbiosis. Here, we report the *de novo* design of a synthetic host defence peptide that targets a specific pathogen by mimicking key molecular features of the pathogen's channel-forming membrane proteins. By exploiting physical and structural vulnerabilities within the pathogen's cellular envelope, we designed a peptide sequence that undergoes instructed tryptophan-zippered assembly within the mycolic-acid rich outer membrane of *Mycobacterium tuberculosis* (Mtb) to specifically kill the pathogen without collateral toxicity towards lung commensal bacteria or host tissue. These 'mycomembrane-templated' assemblies elicit rapid mycobactericidal activity, and enhance the potency of antibiotics by improving their otherwise poor diffusion across the rigid Mtb envelope with respect to agents that exploit transmembrane protein channels for antimycobacterial activity. This biomimetic strategy may aid the design of other narrow-spectrum antimicrobial peptides.

Small-molecule antibiotics are currently our best weapons against bacterial infections. However, their overuse has led to the widespread emergence of multidrug resistance (MDR) and, combined with a lagging discovery pipeline, we now find ourselves quickly running out of useful drugs. An underappreciated, but important, contributor to resistance is the human microbiome.[1] Repeated antibiotic use promotes the accumulation of resistance genes in the overexposed commensal microflora which can then horizontally transfer these genes to colonizing pathogens. Emerging evidence now suggests that population networks enable the exchange of these genes across vast geospatial distances, leading to a globally connected human resistome.[2,3] In the individual, these commensal communities also play important roles in maintaining immune and metabolic homeostasis, as well as preventing opportunistic infections.[4,5] Hence, not only do our microbiomes serve as a long-term reservoir of resistance genes that encourage MDR infections, but their disruption by broad-spectrum drugs has immediate and significant health effects. As a result, many drug discovery campaigns have prioritized the development of pathogen-specific antimicrobials which minimize, or altogether avoid, the use of broad spectrum antibiotics so as to preserve the protective human microbiome, enhance patient outcomes and reduce the spread of resistance.[6–8]

Traditional approaches for the discovery of narrow-spectrum antimicrobials relies on large empirical compound screens. These discovery methods are costly, laborious and hindered by the need for extensive med-chem optimization of lead candidates.[9,10] An alternative strategy is to rationally design antimicrobials that act by mimicking physical features of the target pathogen envelope to generate supramolecular defects in the microbial cell wall. Utilizing native transmembrane proteins as templates, this approach would allow for the development of biomimetic antimicrobials that undergo templated assembly within the target microbial envelope to enable precision killing of pathogens with minimal off-target effects.

Here, we apply this strategy to design a pathogen-specific antimicrobial host defense peptide against *Mycobacterium tuberculosis* (Mtb), the causative agent of Tuberculosis (TB). This is

achieved by rationally engineering the *de novo* peptide to assemble into structures mimicking the mycobacterial specific cell wall porin, MspA. To confer anti-TB specificity, the lead candidate sequence, named myco-membrane associated disruption 1 (MAD1) peptide, was further refined through homology-directed *in silico* design guided by conserved domains in transmembrane protein channels of Mtb, as well as other phylogenetically related bacteria. Complementary atomistic simulations, biophysical analyses and microbiologic assays demonstrate that MAD1 selectively potentiates lysis of the Mtb membrane upon interaction with the mycolic-acid rich outer mycobacterial surface. This enables the peptide to elicit rapid and selective killing of virulent TB pathogens (death occurs in <1 hour) without collateral toxicity towards polymicrobial respiratory commensals and host lung tissue. Further, these membrane-specific mechanisms synergistically enhance the potency of clinical TB antibiotics that otherwise poorly diffuse across the rigid outer myco-membrane of Mtb pathogens.

Biomimetic design of MAD1

The initial design of MAD1 was inspired by the mycobacterial-specific porin MspA. This β-sheet rich, homo-octameric transmembrane protein is unique to mycobacteria and forms a single-channel pore that permits the diffusion of hydrophilic molecules across the outer membrane (Fig. 1a).[11] Importantly, the structure of MspA has evolved to assemble within the distinct environment of the mycobacterial cell envelope, which is defined by an extremely rigid outer membrane that is rich in mycolic acids. Notably, MspA presents a distinctive girdle of tryptophan residues in its membrane-spanning domain that has been specially adapted to localize the porin rim at the mycolipid-water interface (Fig. 1b).[12] These tryptophan-rich features are unique to MspA and are not found in other porins identified in non-mycobacterial microbes.[11] Juxtaposed to this nonpolar outer porin surface is a hydrophilic interior that is rich in basic residues. In addition, arginines 33, 35 and 38 in the subunit loop region extend into the mycolic-peptidoglycan interface (Fig. 1c), suggesting they support anchorage of the porin within the mycolyl-arabinogalactan-peptidoglycan complex.[13] To replicate these molecular features in a host defense peptide, we constructed the thirteen amino acid *de novo* sequence MAD1: KRWHWWRRHWVVW-NH_2. *In silico* design of this scaffold began by constraining the candidate sequence to an α-helix, a common secondary structure of both antimicrobial peptides[14,15] and transmembrane protein domains.[16] The identity and position of each amino acid was then selected based on a functional decomposition BLAST analysis of solute-specific transmembrane channels (e.g. PE and PPE) found in Mtb,[17,18] as well as membrane-associated proteins from other species phylogenetically related to mycobacteria (Supplementary Table 1). This identified homologous motifs within candidate membrane-spanning protein domains, many of which are segments of α-helices. Conserved residues among these sequences were prioritized, and the design of MAD1 further optimized by excluding amino acids known to disrupt α-helical secondary structure and/or which interrupted the facial amphiphilicity of the *de novo* helix (see colored residues in Supplementary Table 1). Molecular simulations of MAD1 suggests it adopts an α-helical conformation defined by a nonpolar tryptophan-rich domain opposed to a charged polar surface (Fig. 1d), thus recapitulating the facial amphiphilicity of MspA and other transmembrane Mtb channels. TOCSY and NOESY NMR analyses support an α-

helical secondary structure in aqueous solutions, most prominently in the C-terminal 7–13 residues of the peptide (Supplementary Figs. 1 & 2). In juxtaposition to this, MAD1's N-terminal lysine and arginine residues adopt extended side-chains analogous to the basic loop of the MspA porin rim subunit (Fig. 1c).

Important to MAD1's biophysical activity are two histidine residues displayed on its polar face. These histidines enable pH-triggered assembly of MAD1 within the acidic phagosome of macrophages (pH 5.5 – 6.0),[19] a key cellular niche for Mtb pathogens during TB infection.[20,21] To demonstrate this, circular dichroism (CD) spectroscopy was performed under various pathophysiological conditions. At pH 7.4, MAD1 displays a CD spectrum suggestive of mixed α-helical (minima at 206nm and 219nm) and β-sheet (minima at 212nm) conformations (Fig. 1e, see inset). An exciton band at 228nm is indicative of interactions between tryptophan aromatic indole chromaphores.[22] TEM micrographs show that at pH 7.4 MAD1 organizes into short fibrils that are 100 – 200 nm in length and ~6 nm in width (Supplementary Fig. 3). Taken together, this suggests that MAD1 helices, estimated to be ~1.7 nm in the axial dimension, undergo Trp-Trp intermolecular pairing at physiologic pH to form laminated proto-fibrillar assemblies. Under acidic conditions, however, MAD1 evolves an unusual CD spectrum with intense exciton-coupled bands at 212 and 228 nm (Fig. 1f), a profile analogous to a putative tryptophan zipper.[22,23] While such Trp-zippers are most often associated with stabilization of β-hairpins, their contribution to helix association in supramolecular coiled coil structures has been reported.[24] Importantly, this spectrum closely matches that of the full-length recombinant MspA protein, which displays similar exciton bands at 216 and 230nm.[25] TEM imaging reveals that under these conditions MAD1 zippers into monomorphic amyloid-like fibers approximately 300 – 700 nm in length and 5.5 nm in width (Fig. 1g, Supplementary Fig. 4). Collectively, our data at both pH 7.4 and 4.5 indicate that MAD1 undergoes supramolecular assembly to form tryptophan-zippered architectures similar to the β-sheet rich features of the MspA template from which the peptide was designed.

Plotting the pH-dependent elliptical change resulting from MAD1's β-sheet (θ_{212nm}) and tryptophan-zipper (θ_{228nm}) structures demonstrates that the peptide's supramolecular conformational equilibrium shifts at pH < 6.0 (Fig. 1h). This aligns with the pKa of histidine's imidazole side chain and supports our assertion that these residues may play an important role in directing MAD1 fibrilization in acidic microenvironments (e.g. macrophage phagosome). Yet, given the polycationic nature of MAD1 it is unusual that its self-assembly would be driven by acidic conditions, rather than disrupted due to intermolecular electrostatic repulsion. In nature, pathway driven self-assembly is a composite of noncovalent forces and solvation effects that direct divergent intermolecular interactions, leading to the potential emergence of nonequilibrium states.[26,27] To investigate the thermodynamic stability of MAD1 nanostructures, *en route* to understanding the mechanistic basis for its potential nonequilibrium assembly behavior, we performed thermal change CD studies. MAD1 displays a reversible thermal denaturation curve (T_m = 39°C) with forward and reverse melting profiles that are closely overlaid (Fig. 1i, Supplementary Fig. 5). Taken together, our data suggests that MAD1's fibrillar state may exist as a manifold of reversible tryptophan-zippered conformations. Thermodynamically favored states may be more accessible upon increased conformational flexibility of monomers mediated by intra-

and inter-molecular electrostatics. This assertion was next tested through rigorous *in silico* experiments.

MAD1 conformational dynamics

To elucidate the atomistic mechanisms underlying MAD1 self-assembly we performed discrete molecular dynamics (DMD) simulations of the peptide in the unprotonated (pH > 6.0) or protonated (pH < 6.0) histidine state. In agreement with experiments, we find the peptide monomer forms an α-helical structure (Fig. 2a), with similar backbone but differing side chain orientation at the two pHs. Under acidic conditions, MAD1 is highly dynamic, exhibiting significantly increased root mean square fluctuations (RMSF) over the length of the peptide. Although the static structure of MAD1 is similar at acidic and neutral pH, these heightened dynamics suggest decreased thermodynamic stability at pH < 6. Using replica exchange simulations, we observe that the melting curve of MAD1 at acidic pH shifts to the left (Fig. 2b), confirming decreased stability when the peptide's histidine side chains are protonated. This decreased thermodynamic stability may increase propensity for aggregation, possibly explaining the fibrils observed in our TEM experiments (Fig. 1g). To test this propensity *in silico*, we performed simulations of five peptides in solution at both acidic and neutral pH. We found that not only are the individual peptides more dynamic in acidic environments, even when assembled into a pentamer (Fig. 2c, left), but that assembly is more chaotic and the structural space of potential pentamers is more highly degenerate, as evidenced by comparison of structures resulting from ten randomized simulation iterations (Fig. 2c, right). Further, we found that this structural plasticity in MAD1 pentamers exhibited more frequent residue-residue contacts at acidic pH (Fig. 2d, bottom diagonal). The structural plasticity was also reflected across tryptophan-tryptophan residue contacts at acidic pH (Fig 2e, bottom diagonal). Increased frequency of tryptophan-tryptophan interactions at low pH reflects promoted formation of a tryptophan zipper motif (Fig. 2e, bottom diagonal). In contrast, we observe fewer, but stronger, interactions at neutral pH, suggesting a less diverse ensemble of structural states (Fig 2d & e, top diagonals). To further explore these atomistic mechanisms of peptide assembly, we examined structural states of MAD1 at energetic transitions (Fig. 2f). Similar energetic states were identified of approximately −330 kcal/mol (fully assembled pentamer), −205 kcal/mol (partially assembled pentamer), and −125 (pH 7) or −105 (pH 5.5) kcal/mol (dissociated monomers maintaining at least partial secondary structure). The shift toward higher energy in this dissociated structure denotes decreased stability of separated monomers at pH < 6. Together, this demonstrates that increased conformational flexibility of MAD1 at acidic pH, caused by intramolecular electrostatic repulsion, favors more dynamic intermolecular interactions relative to neutral conditions, which in turn confers a higher energetic benefit to assembly and a greater barrier to dissociation once oligomers have formed. This has pathophysiologic significance as the pH of the macrophage phagosome, where Mtb reside during infection, evolves from pH 6.2 to 4.5 after microbial ingestion.[19,28] This suggests that triggered assembly of MAD1 in the acidic phagosome may protect the peptide from hydrolytic and/or enzymatic neutralization, thus maintaining its activity against TB pathogens that exploit this acidic host niche for survival.

Antituberculosis specificity via myco-favored interactions

Bactericidal specificity of MAD1 was next determined against a diverse microbiologic panel containing virulent mycobacteria, as well as a variety of Gram-negative and Gram-positive lung commensals and pathobionts. Results in Table 1 demonstrate that MAD1 elicits potent activity towards its Mtb target, with a minimum inhibitory concentration (MIC) similar to many first-line TB antibiotics (MICs ~ 0.5–20 μM).[29] Given the pH-dependent assembly behavior of MAD1, we also performed two complementary MIC assays to examine the impact of microenvironmental acidity on peptide activity. The first measured MAD1's MIC towards Mtb at varying broth pH (5.5 – 7.5), and the second pre-assembled MAD1 in an acidic buffer before addition to physiologic TB cultures (pH 7.4). In both settings, MAD1 retains its low micromolar potency (Supplementary Table 2), suggesting that the peptide will not be neutralized in the acidic macrophage phagosome. Mtb clearance assays performed in TB-infected macrophages affirm this assertion, as described in later studies. In addition to its ability to kill Mtb, MAD1 was also effective towards *Mycobacterium bovis* (*M. bovis*) and *Mycobacterium smegmatis* (*M. smegmatis*), the latter a non-pathogenic mycobacteria defined by abundant MspA content in its cellular envelope. As MAD1 is designed to physically disrupt the outer membrane of these mycobacteria, which is a mechanism not shared by conventional TB antibiotics, we also tested the peptide's activity against a mutant *M. bovis* strain (TMC 1103) resistant to the front line antibiotic isoniazid. As anticipated, MAD1 shows equal potency towards drug-resistant *M. bovis* as it does towards the other tested mycobacteria, with an MIC of 5 μM (see *M. bovis (INH-R)* in Table 1).

Remarkably, MAD1 displays an exceptional myco-specificity relative to other Gram-negative and Gram-positive respiratory commensals tested in the panel, with a selectivity index (SI) of 20. This specificity is an order of magnitude greater than three other tryptophan-rich, antimycobacterial peptides tested, which were selected based on their reported anti-TB activity (AMPs1–3 in Table 1).[30] MAD1 is similarly discriminatory when compared against many second-line TB antibiotics, which generally have SI's ≤ 2.[29]

To test the importance of chirality on MAD1 bioactivity we prepared an analogue of the peptide using non-natural *D*-amino acids (Supplementary Fig. 6), and screened the enantiomer against the bacterial panel (Table 1, MIC in parenthesis). Surprisingly, although *D*-MAD1 showed similar potency as its *L*-analogue towards mycobacteria, the enantiomer did not retain the same antitubercular specificity. This suggests that MAD1's ability to distinguish mycobacteria from commensal microbes is conferred through a chirality-sensitive, physical mode of action. These interactions may be mediated through the templated organization of the peptide into natural *L*-chiral assemblies within the mycolic acid-rich cell envelope.

To further investigate a membrane composition-dependent mechanism of action, we next examined the conformational dynamics of *L*-MAD1 in the presence of liposomal myco-membrane models (Fig. 3a). CD spectra presented in Fig. 3b shows a slight, transient loss of MAD1's helical and β-sheet conformational states ($\theta_{200–220nm}$) upon interaction with membranes prepared from the Mtb cell envelope glycolipid, trehalose dimycolate. Plotting the magnitude change in MAD1 β-sheet structure (θ_{212nm}) reveals this transition peaks at 10

minutes, and then reverses to restore its initial sheet-rich architecture (Fig. 3c). Conversely, MAD1 is rapidly denatured upon mixing with both the Gram-positive and Gram-negative model membranes, and is unable to recover its secondary structure over the remainder of the experiment (Fig. 3b and c). In separate studies, optical density measurements were used to monitor the disruption of each bacterial membrane in the presence of elevated MAD1 concentrations. Results in Fig. 3d demonstrate that nearly 100% of myco-membranes are lysed within ten minutes following the addition of the peptide. Interestingly, this rapid lytic action matches the kinetics of MAD1's conformational states upon myco-membrane insertion (Fig. 3c), suggesting a direct link between peptide structure and myco-lytic potential. Under similar conditions MAD1 elicits modest disruption of Gram-positive and Gram-negative liposomes (~58% and ~33%, respectively) and is weakly active towards mammalian control membranes prepared from lipid compositions matching healthy lung epithelium (−3% change, see Supplementary Fig. 7). These results provide strong evidence for the selective interaction of MAD1 with myco-membranes, further supported by a co-sedimentation assay indicating avid binding of mycolic acids to MAD1 (Supplementary Fig. 8). Taken together, our data demonstrate the potential for MAD1 to preferentially bind to, and assemble within, mycomembranes to precisely kill Mtb pathogens in polymicrobial commensal environments without damage to healthy host tissue; an assertion we validate in later studies.

Although our results clearly demonstrate myco-specific action of the peptide, the modest disruption of Gram-positive membranes by MAD1 appears to contradict its near complete inactivity towards Gram-positive microbes in our bacteriologic assays (Table 1). These divergent results may be a consequence of the lack of a peptidoglycan layer in our model liposomes. This is important because, while both organisms share a similar inner membrane composition, Gram-positive microbes have a multi-layered peptidoglycan coating that is generally thicker than that of mycobacteria.[31,32] This dense glycan interface may preferentially adsorb MAD1 and prevent its ability to partition to the inner membrane, thus insulating Gram-positive lung commensals from peptide-mediated lysis. Supporting this assertion, plasmon resonance (SPR) experiments demonstrate that MAD1 avidly binds peptidoglycans isolated from the Gram-positive commensal *S. aureus* (K_D = 9 μM; Supplementary Fig. 9). Similarly, *L*-MAD1's activity towards the Gram-positive bacterium *B. subtilis* is reduced by 8-fold in a mutant strain (PY79) that possesses a significantly thicker peptidoglycan layer relative to the 168 wild-type (Supplementary Table 3). This strain-dependent specificity was again lost when testing the *D*-MAD1 enantiomer. These results support a fundamental role of peptidoglycans in protecting non-mycobacterial commensals from the action of MAD1, and suggest an *L*-chiral dependence of these peptide-glycan interactions.

Mtb-instructed MAD1 assembly into supramolecular nano-lytics

Thus far, our *ex cellulo* experiments demonstrate that MAD1's lytic activity is conferred via its preferential interactions with mycolic acids. We next explore if these same membrane-templated lytic phenomena occur in the context of living Mtb cells, first through a fluorometric permeabilization assay. Here, we use the membrane potential sensitive dye 1-N-phenylnaphthylamine (NPN), which is excluded from intact membranes but enters

damaged phospholipid layers to display prominent fluorescence.[33–37] As expected, treating Mtb with increasing concentrations of MAD1 resulted in a corollary enhancement of NPN fluorescence in a dose-dependent manner (Fig. 4a). Time-dependent fluorescence measurements indicate this MAD1-mediated mycomembrane permeabilization occurs within a few minutes of exposure (Supplementary Fig. 10).

To corroborate these results, we investigated Mtb membrane dynamics in the presence of MAD1 through a series of label-free impedance spectroscopy (IS) experiments. This technique measures the current between two electrodes induced by an alternating voltage to calculate a complex impedance, $Z(\omega)$, where ω is the voltage frequency.[38,39] When applied to bacterial cells, frequency-dependent changes in impedance can be used to infer properties of the extracellular and intracellular milieu upon treatment with MAD1. To facilitate interpretation of this complex system we use a generalized biologic circuit (Fig. 4b) and designed two complementary experiments to study MAD1-mediated changes in Mtb membrane integrity. In the first study (Fig. 4c, black bars), we employ low frequency electric fields to measure changes in supernatant impedance (ΔZ) upon treatment of Mtb with MAD1, which can be used to infer cytoplasmic leakage of ions into the extracellular space. As expected, we observed a decrease in the extracellular solution impedance (equivalently the resistance) as intracellular ions escape the MAD1-permeabilized mycobacterial envelope (processed impedance spectra, and associated raw data, are shown in Supplementary Figs. 11 and 12, respectively). In the second experiment (Fig. 4c, grey bars), a high frequency electric field is employed that, in contrast to low frequencies, penetrates the mycobacterial envelope to directly measure cytoplasmic impedance. Results show that ΔZ of the Mtb cellular compartment increases following treatment with the peptide, indicating a loss of intracellular ionic content (i.e. an increase of cytoplasmic resistance) due to cell envelope damage. Recent dielectrophoresis studies have similarly shown that mycobacterial cell envelope capacitance and cytoplasm conductivity decrease (hence, ΔZ increases) upon treatment with heat or the antibiotic isoniazid, both of which induce morphological cell wall changes.[40] These previously reported results, together with our findings, strongly support a membrane-directed antitubercular mechanism of action for MAD1 that compromises Mtb envelope integrity to elicit rapid mycobactericidal activity.

In separate studies, we utilized confocal and electron microscopy to directly probe MAD1 localization to the Mtb cell surface, and investigate peptide-mediated morphologic changes in the myco-envelope architecture upon interaction. Fluorescence microscopy revealed that MAD1 rapidly localizes to the Mtb cell wall within 15 minutes of exposure (Supplementary Fig. 13). When employed at sub-lytic concentrations (0.1 x MIC), these outer membrane interactions cause the typically smooth Mtb bacterial surface to display a ruffled morphology that is complemented by the formation of extracellular aggregates (Fig. 4d). Increasing the concentration of MAD1 to 0.5x – 5x its MIC led to a stark change in cell surface morphology characterized by the formation of pitted architectures and delamination of the cell wall (Fig. 4d and Supplementary Fig. 14). Remarkably, close inspection of the Mtb cell surface reveals the formation of MAD1 cylindrical assemblies that are ~14 nm in diameter (Figure 4d, magnified image and inset), which approximates the size of the MspA porin head (9 nm in width).[41] Fluorescent microscopy indicates that these assemblies

sufficiently destabilize the outer mycomembrane to allow the intracellular diffusion of the otherwise membrane-impermeable dye propidium iodide (Supplementary Fig. 15). SEM and confocal images also revealed a propensity for MAD1 to agglutinate treated Mtb cells (Fig. 4d and Supplementary Fig. 16), similar to the behavior of amyloid-like self-assembling antimicrobial peptides.[42,43]

To probe intracellular changes in Mtb cells following exposure to MAD1, TEM imaging was performed on bacilli treated with increasing concentrations of the peptide (Fig. 4e). At low MAD1 concentrations (0.1 x MIC), cytoplasmic granules begin to develop indicative of an early cellular stress response. At elevated peptide concentrations (0.5x – 5 x MIC) a low-density corona is observed circumscribing the treated Mtb cell (Fig. 4e and Supplementary Fig. 17, white space around cell). This electron-deficient outer halo is most likely formed due to MAD1-mediated exfoliation of the outer mycobacterial membrane. Additionally, we observed a significant amount of cellular debris forming in the extracellular space when treated at high peptide concentrations. This further corroborates data from impedance spectroscopy, as well as our confocal and SEM imaging studies, and together strongly supports a mechanism of MAD1-mediated envelope poration and cell agglutination. Nevertheless, we cannot exclude the possibility of an additional intracellular target of the peptide, particularly as we observe internalization of MAD1 following initial cell wall destabilization (Supplementary Fig. 15). These potential intracellular interactions are being explored in follow up work.

Polymicrobial specificity, macrophage clearance, and synergy

In separate studies, we tested the ability of MAD1 to selectively engage its mycobacterial target in a complex polymicrobial milieu. In initial experiments, Mtb cells were mixed with the Gram-positive and Gram-negative commensals *S. aureus* and *K. pneumoniae*, respectively, before addition of the MAD1 peptide. Treated cultures were subsequently labeled with auramine-rhodamine, a fluorescent dye that selectively accumulates in healthy, acid-fast mycobacteria.[44] Like NPN, this dye enables specific interrogation of Mtb cell integrity in the mixed commensal population. Results in Fig. 5a show a significant decline in Mtb integrity as MAD1 concentration is increased from 1.0x – 10 x MIC. In parallel experiments, Mtb-specific killing was tested by comparing the growth rate of Mtb against co-treated commensals in the presence of MAD1. To select an appropriate peptide dose, cytotoxicity curves were generated for each species as a function of increasing MAD1 concentration (Supplementary Fig. 18). These curves identified a therapeutic window for MAD1 of 2 – 20 μM, between which complete killing of Mtb is achieved without significant toxicity towards the commensals *S. aureus* and *K. pneumoniae*. Choosing a MAD1 concentration within this range, 10 μM (4 x MIC_{Mtb}), we next treated each strain with the peptide and monitored their time-dependent growth. Results in Fig. 5b show that the proliferation rate of *S. aureus* or *K. pneumoniae* commensals was not changed upon addition of the peptide. Conversely, Mtb growth was completely inhibited in culture by the MAD1 peptide.

In parallel experiments, MAD1 was found to be well tolerated by a panel of cell lines with pathophysiologic relevance to pulmonary TB, including NL-20 (human lung epithelium),

THP-1 (human monocyte), RAW 264.7 (murine macrophage), and human vascular endothelial cells (HUVEC). All four cell lines remained viable when treated with concentrations of MAD1 well above its MIC_{Mtb} (see dashed line in Fig. 5c), resulting in therapeutic indices of 30 – 54 (Supplementary Table 4). Moreover, intracellular killing assays performed in Mtb-infected RAW 264.7 macrophages demonstrate that MAD1 treatment leads to a statistically significant reduction of Mtb persister burden at peptide concentrations ≥1 x MIC (2.5 μM), with minimal collateral toxicity towards the macrophage hosts (Fig. 5d). Collectively, our bacteriologic and mammalian cell data strongly suggests that MAD1 maintains its myco-membrane targeted mechanism of action in complex cellular mixtures, leading to precise anti-TB activity without significant collateral toxicity of lung microflora or host tissue.

Finally, given MAD1's ability to selectively permeabilize the rigid outer mycobacterial envelope, we employed checkerboard assays to assess the peptide's potential to synergistically enhance the efficacy of select first- and second-line TB antibiotics. This has important clinical implications as poor intracellular permeation of many TB drugs necessitates high doses and long treatment durations to achieve successful clinical outcomes. As shown in Fig. 5e, MAD1 displays additive effects with first-line agents isoniazid (INH), ethambutol (EMB) and rifampicin (RIF), and potently synergizes with the second-line agent moxifloxacin (MOX). Interestingly, previous work has shown that Msp porins facilitate diffusion of MOX into mycobacteria and contributes to its antitubercular effects.[45] Correspondingly, *M. smegmatis* deletion mutants that lack the ability to express Msp porins have a pronounced resistance to MOX compared to the wild-type strain. This suggests that MAD1 may synergistically enhance the activity of MOX by forming supramolecular defects in the Mtb envelope that potentiates improved intra-bacilli transport of the antibiotic.

Discussion

We have established a biomimetic design strategy that can be used to directly prototype *de novo,* pathogen-selective host defense peptides. This approach eliminates the need for large empirical screens and, hence, allows for a robust and rapid antimicrobial discovery pipeline. A unique advantage of this methodology is that narrow-spectrum peptides may be produced at-scale using insensitive bacterial expression systems (MAD1 for example is weakly active towards *E. coli*); a production method that is otherwise inaccessible to naturally-derived broad-spectrum antimicrobials. More importantly, this strategy can be used to develop antimicrobials that do not target a particular biochemical pathway, but instead act by exploiting physical structural features of the cell envelope that may be difficult for pathogens to mutationally alter.

As an exemplary application we have prepared a TB-specific host defense peptide, MAD1, initially inspired by the mycobacterial-specific porin MspA and refined through molecular features conserved in Mtb-specific outer membrane proteins. MAD1 organizes into tryptophan-zippered supramolecular assemblies that recapitulate the β-sheet rich architecture of the porin template from which it was derived. We show that this biomimetic behavior confers MAD1 with the ability to selectively target the mycolic-acid rich surface of Mtb to elicit rapid and precise anti-TB activity. Biophysical and microscopy studies also

suggest MAD1's antitubercular effects may be mediated, in part, through Mtb cell agglomeration. Similar phenomena have been observed for amyloid-like self-assembled peptide structures, which evolve fibrillar lattice networks that physically trap nearby bacteria rather than direct killing of the invader.[46–48] Collectively, these membrane active mechanisms of MAD1 serve to potentiate the activity of other drugs against Mtb by permeabilizing the rigid myco-envelope that otherwise inhibits the intracellular partitioning of antibiotics, and can specifically aid the pore-mediated diffusion of fluoroquinolones into mycobacteria. Together, these results warrant additional preclinical studies to evaluate MAD1's safety and efficacy, along with comprehensive genetic experiments to inform on the peptide's combinatorial mode of action and frequency/mechanism of resistance.

Interestingly, nature appears to have adopted a tangential strategy in the evolution of antimicrobial peptides, generating biologics that kill Gram-negative cells by binding to and inhibiting β-barrel outer membrane proteins,[49,50] or lipoproteins involved in β-barrel folding and outer membrane biogenesis.[50,51] For example, the insect-derived antimicrobial peptide thanatin has been shown to inhibit protein-protein interactions between Lpt subunits in *E. coli*, a lipopolysaccharide-transporting complex required for outer membrane biogenesis in Gram-negative bacteria.[49] Peptidomimetics derived from the polymyxin and colistin family of natural products have also been shown to kill Gram-negative ESKAPE pathogens by binding to the main component (BamA) of the β-barrel folding complex BAM.[51] These examples highlight an emerging class of outer membrane targeted antibacterials, and suggest porin-mimetic supramolecular peptide assembly may represent a unique, and complementary, paradigm in the design of pathogen-specific agents. Although applied here to TB, there are numerous pathogens with varied channel-forming membrane proteins with which to rationally design biomimetic antimicrobials. Therefore, this work may enable the development of precision antimicrobials capable of combating MDR respiratory infections without impacting lung commensals and host tissue.

Methods

Materials.

Lysogeny broth, Mueller Hinton broth, 7H9 media, formic acid, Acetonitrile, auramine/rhodamine, decolorizer, potassium permanganate counterstain, HCl, dichloromethane, 1,2-Ethanedithiol, diethyl ether, 1,3-bis(tris(hydroxymethyl)methylamino)propane (BTP), piperadine, spec dmso, thioanisole, sodium fluoride, sodium hydroxide, dimethyl sulfoxide cell culture grade (DMSO), biotech CE dialysis tubing (MWCO 300kD), Gram Stain, DMEM, 96 well tissue culture plates L-glutamine, FBS, trypsin and RPMI media were purchased from ThermoFisher Scientific. Anisole was purchased from Tokyo Chemical Industry. Dimethylformamide, ethanol, F12 media, gentamycin, sodium phosphate monobasic and sodium phosphate dibasic were purchased from VWR. Glycerol, tween 80, OADC growth supplement, BHI, *S. aureus* peptidoglycans, DiOC2(3), sterile ThermalSeal films, Triton X-100, MEM non-essential amino acid solution, D-(+)-Glucose, Insulin (Recombinant human), Transferrin Apo- (human plasma), EmbryoMax Ultrapure Water with 0.1% Gelatin, hydrocortisone and sodium bicarbonate were purchased from Millipore-Sigma. Fmoc-protected amino acids, rink amide resin, Oxyma, DIC, 3-(4,5-dimethyl-2-

thiazolyl)-2,5-diphenyl-2H-tetrazolium bromide (MTT), N,N^0-diisopropylcarbodiimide (DIC), OG surfactant and Trifluoroacetic acid were purchased from Chem-Impex Int. 2-dioleoyl-sn-glycero-3-phosphoethanolamine (DOPE), 1,2-dioleoyl-sn-glycero-3-phospho-(1'-rac-glycerol) (DOPG), cardiolipin (CL) and 1-Palmitoyl-2-oleoyl-sn-glycero-3-phosphocholine (POPC) lipids were purchased from Avanti. SPR carboxy-functionalized chips were purchased from Reichert. Trehalose-6,6-dimycolate (TDM) was purchased from InvivoGen.

BLAST search and sequence design.

BLASTp searches were preformed using the Actinomycetales sub-order Corynebacterineae, the Mycobacteriaceae family, the *Mycobacterium* genus and specific organism *M. tuberculosis* to filter. Alignments were further refined through manual substitution of amino acids known to disrupt helices (e.g. Gly, Pro),[52,53] or acidic/uncharged residues reported to decrease antimicrobial potency (e.g. Asp, Glu, Asn, Gln).[54,55] The residues were substituted with tryptophan, arginine or lysine, with identity and positioning selected to maintain amphiphilic facial character and helical structure.[56]

Cell lines and culture conditions.

HUVEC, THP-1, Vascular Cell Basal Medium and the Endothelial Growth Cell Kit–VEGF were purchased from ATCC. NL20 cell line was generously gifted by the laboratory of Matthew Taylor, Penn State University, College of Medicine. NL20 (CRL-2503) cells were cultured in Ham's F12 as recommended by ATCC. HUVEC (PCS-100-010) were cultured in supplemented Vascular Cell Basal Medium and grown in flasks coated for 15 min at 37 °C with 0.1% gelatin. THP-1 (TIB-202) cells were cultured in RPMI-1640 medium supplemented with 10% FBS and 50 mM 2-mercaptoethanol (BME). All above cultures were maintained at 37 °C under 5% CO_2 with 0.1% gentamycin. RAW 264.7 cell line was generously gifted by the laboratory of Yong Wang, Penn State University, Department of Biomedical Engineering. RAW 264.7 murine macrophages (TIB-71) were cultured in antibiotic-free RPMI-1640 medium supplemented with 10% FBS. Bacterial strains and culture conditions were obtained from ATCC.

Peptide synthesis.

Peptides were synthesized by Fmoc-based solid-phase peptide synthesis on Rink Amide ProTide resin. 1M Oxyma and 0.5M N,N′-Diisopropylcarbodiimide (DIC) were used for activation and the synthesis was carried out in a Liberty Blue Automated Microwave Peptide Synthesizer (CEM, Matthews, NC). AMP2 and AMP3 were synthesized with 0.1M N, N-Diisopropylethylamine (DIEA) in the Oxyma solution and 1M DIC. Fluorescently labeled peptide was prepared by further reacting MAD1, on resin, with 2 equivalents of NHS-Fluorescein (5/6-carboxyfluorescein succinimidyl ester) and 4 equivalents of diisopropylethalamine in DMF, and allowed to shake at room temperature for 4 hours. Reaction progress was monitored with the Kaiser test to detect free amines. Resin cleavage and side-chain deprotection was performed under argon using a trifluoroacetic acid:thioanisole:1,2-ethanedithiol:anisole (90:5:3:2) solution while stirring for 2 hours (AMP1), 3 hours (AMP2, AMP3) and 3 hours at 30°C (MAD1). Crude peptide was

subsequently precipitated with cold (4°C) diethyl ether and isolated by centrifugation at 5000 rpm for 5 minutes. Diethyl ether was decanted and sample lyophilized overnight.

Peptides were purified by reverse-phase HPLC (Shimadzu, Columbia, MD) equipped with a Phenomenex Semi-Prep Luna Omega PS C18 column (Torrance, CA). Analytical LCMS solvents consisted of solvent A (0.1% formic acid in water) and solvent B (9:1 acetonitrile and water with 0.1% formic acid). Preparative HPLC solvents consisted of solvent A (0.1% trifluoroacetic acid in water) and solvent B (9:1 acetonitrile and water with 0.1% trifluoroacetic acid). A linear gradient of 0–25% solvent B over 25 minutes followed by 25–45% solvent B over an additional 40 minutes was used to purify *D*/*L*-MAD1 and AMP2. A linear gradient of 0–45% solvent B over 45 minutes was used to purify AMP1. A linear gradient of 0–25% solvent B over 15 minutes followed by 25–45% solvent B over an additional 40 minutes was used to purify AMP3. After lyopholization to collect pure peptide, all compounds were characterized by LC-MS ESI (+) to define purity (Supplementary Figs. 19 – 24).

Bacterial growth.

Mycobacterium tuberculosis (H37Ra and H37Rv) and *Mycobacterium smegmatis* (mc^2 155) were cultured in Middlebrook 7H9 broth supplemented with 0.05% (v/v) polysorbate 80, 0.5% (v/v) glycerol and 10% (v/v) oleic acid-albumin-dextrose-catalase (OADC). *Mycobacterium bovis* (TMC 1012 and TMC 1103) was isolated on Lowenstein-Jensen medium and cultured in supplemented Middlebrook 7H9 broth with 40 mM sodium pyruvate. Methicillin resistant *Staphylococcus aureus* (MRSA; USA300), Methicillin sensitive *Staphylococcus aureus* (MSSA; NRS72), *Klebsiella pneumoniae* (NCTC 9633), *Salmonella enterica* (ATCC 14028), *Pseudomonas aeruginosa* (POA-1) and *Acinetobacter baumannii* (ATCC 19606) were cultured in cation adjusted Mueller-Hinton broth (CAMHB). *Staphylococcus aureus* (Newman), *Bacillus anthracis* (Sterne 34F2), *Bacillus subtilis* (168 and PY79) and *Escherichia coli* (DH5α) were cultured in lysogeny broth (LB). *Streptococcus mitis* (NCTC 12261), *Enterococcus faecalis* (ATCC 29212), *Haemophilus influenzae* (ATCC 49247) was cultured in brain heart infusion (BHI). All cultures were grown at 37°C in a shaking incubator (200 rpm), as advised by the Clinical and Laboratory Standards Institute (CLSI).

Liposomal membrane preparation.

Liposomes were formed using extrusion techniques as previously described.[57,58] In brief, Gram-positive, Gram-negative and mammalian model membranes were prepared by combining appropriate combinations of lipids in chloroform to a final concentration of 5 mM. Lipid solution was then dried under a stream of argon, and film lyophilized overnight to dry completely. The film was rehydrated with 2x concentrated liposome buffer (300 mM BTP, 100 mM NaF, pH 7.4). The solution was then extruded through an Avanti Mini Extruder (Alabaster, Alabama) with a 0.8 μm nuclepore polycarbonate membrane >11 times. For Gram-positive membranes, a mixture of DOPG and CL (58:42) was used to mimic *Staphylococcus aureus*.[59] For Gram-negative membranes, a mixture of DOPE:DOPG:CL (65:23:12) was used to mimic *Pseudomonas aeruginosa*.[60] For mammalian membranes, a mixture of POPC:DOPE (3:1) was used to model a typical lung epithelial cell.[61] For

mycomembrane models, Trehalose-6,6-dimycolate (TDM) was solubilized at 2.5 mg/mL in 10% n-Octyl-β-D-glucopyranoside (OG) as a surfactant and vortexed. The solution was then extruded through an Avanti Mini Extruder (Alabaster, Alabama) with a 0.1 μm nuclepore polycarbonate membrane >11 times. Following extrusion, all liposome formulations were dialyzed against 10 μM phosphate buffer for 24 hours using 300 kDa MWCO dialysis tubing. Dynamic light scattering (DLS) was performed to ensure uniform particle sizes for each liposomal composition (Supplementary Fig. 25).

Minimum inhibitory concentration determination.

Bacterial growth was monitored by performing optical density (OD) readings at 600 nm (OD_{600}). Triplicate 2-fold serial dilutions of each treatment were made in strain appropriate media and added to a 96-well microtiter plate.[62] Bacteria were diluted to an OD_{600} of 0.002 and added directly to the treated wells in a 1:1 volume ratio. The microtiter plates were incubated at 37 °C, and bacterial growth was assessed by visual evaluation. Treatment lasted 48 hours for *M. smegmatis* and *M. bovis*, and 96 hours for *M. tuberculosis*, as determined by doubling time. Treatment lasted 24 hours for all other bacterial strains tested. The minimum inhibitory concentration (MIC) was determined by observing the lowest concentration at which the compound prevented significant growth as compared to the untreated control. Concentrations relative to MIC in subsequent experiments were adjusted to bacterial OD. Assays were repeated on at least 3 separate genetic populations ($n \geq 9$), and the lowest repeatable MIC is reported.

To assess the effect of pH on MAD1 toxicity, 7H9 broth was adjusted to a pH range from 5.5 – 7.4, using a previously described protocol.[63] The adjusted media was then used for all treatment and bacterial dilutions. Cells treated at pH 5.5 were incubated for 6 days before reading MIC. 7H9 broth was adjusted to pH 4.5 to pre-form fibrils at high MAD1 concentrations in separate experiments, before treatment at pH 7.4 for the duration of the assay.

Circular dichroism.

CD analysis was performed using a J-1500 Circular Dichroism Spectrometer (JASCO, Oklahoma City, OK). In a typical experiment, 20 μM peptide in 10 mM phosphate buffer at pH 7.4 was added to a 10 mm path length quartz cell and wavelength spectra collected from 180 to 260 nm at 25 °C.[64] Molar ellipticity $[\theta]$, measured in $\left(10^3 \cdot deg \cdot cm^2 \cdot dmol^{-1}\right)$, was calculated from the following expression: $mdeg/(10 \cdot L \cdot C)$ where mdeg is measured ellipticity in millidegrees, L is path length in centimeters, C is molar concentration. CD spectra with 3 technical replicates were collected with $n > 5$ independent experimental replicates on separate days. For pH-dependent CD studies, MAD1 was dissolved at 20 μM in pH adjusted phosphate buffer. This process was replicated on separate days in two independent experiments. Temperature-dependent CD was performed at pH 4.5 by increasing the temperature from 0°C to 90°C at 5 degree intervals, allowing 3 minutes of equilibration before measurements were taken. The reciprocal ramp down was subsequently performed with a similar step interval.

For liposomal CD studies, liposome solutions were diluted to a total lipid concentration of 240 μM in phosphate buffer before mixing with an equal volume of 40 μM MAD1. CD wavelength spectra were measured from 180 to 260 nm at 37°C in a 10 mm path length quartz cell. Measurements were performed immediately after addition of peptide, every 5 minutes until 30 minutes after addition, every 15 minutes until 60 minutes after treatment and every 30 minutes thereafter. The solution was mixed by pipette between each measurement. In a paired experiment, the same sample preparation was used, with OD_{600} measurements being collected.[65] Time points were set at every minute for 15 minutes, every 5 minutes until 30 minutes, and every 30 minutes thereafter. All CD measurements were performed with an average of three technical replicates.

All-atom Discrete Molecular Dynamics simulations.

A complete description of the DMD algorithm can be found elsewhere.[66,67] Briefly, DMD uses discrete step function potentials to model particle-particle interactions instead of continuous functions used in traditional molecular dynamics. This discretization allows instantaneous change in velocity upon collision of particles according to the conservation of energy, momentum, and angular momentum. Implementation of a collision table to track possible collisions, shortening simulation time step to 50 fs, from 2 fs common in traditional molecular dynamics. These innovations significantly decrease computational time, allowing us to achieve a significant increase in sampling. We use an all-atom protein model,[68] which explicitly represents all heavy atoms and polar hydrogens, using infinite square-well constraints to represent bond lengths, angles, and dihedrals. Non-bonded interactions are adapted from the Medusa force field,[69] van der Waals interactions are modeled using the Lennard-Jones potential, solvation is modeled by the Lazaridis-Karplus solvation model,[70] and hydrogen bonding interactions are modeled by the reaction algorithm.[71]

Model systems.

The linear MAD1 peptide was created using PyMol (Shrödinger), and allowed to fold in equilibrium simulations at temperature 0.55 (monomer) or 0.4 (pentamer) kcal/(mol k_B)$^{-1}$ for 100 ns. Pentamer simulations were initialized with randomized relative orientations of the five folded peptides, with no initial contact. Systems were simulated at constant volume with periodic boundary conditions in a 100-angstrom cubic box. Acidic pH (5.5) was modeled by protonation of histidine residues.

Replica exchange.

We used the replica exchange method to perform parallel simulations of the simulation system at multiple temperatures spanning the melting curve of the protein.[72,73] At intervals of 5 ps, replicas of neighboring temperatures exchange temperature values according to the Metropolis criterion, increasing sampling efficiency by increasing ability to overcome energetic barriers. For MAD1 monomer simulations, 10 replicas were used at temperatures of 0.330, 0.360, 0.400, 0.430, 0.460, 0.505, 0.540, 0.580, 0.620, and 0.640 kBT. For MAD1 pentamer simulations, 16 replicas were used at temperatures of 0.340, 0.360, 0.380, 0.400, 0.420, 0.440, 0.460, 0.480, 0.500, 0.520, 0.540, 0.560, 0.580, 0.600, 0.620, and 0.640 kcal/(mol k_B)$^{-1}$. Each replica simulation is performed for 100 ns, for a total of 1 μs (monomer) or 1.6 μs (pentamer).

WHAM analysis and identification of structural transition states.

We combine replica trajectories using the MMTSB tool[74] for weighted histogram analysis method (WHAM) for analysis of folding dynamics.[75] WHAM computes the density of states by combining histograms from overlapping simulation trajectories. We calculate potential energy distributions over each simulation using intermediate temperatures so as not to introduce structural aberrations in representative structures from low- and high-temperature conditions. We identified three peaks and/or shoulders in the distribution, and identify the energy of each state as the histogram peak. We identify representative structures of each state by clustering structures whose energies fall within 5 kcal/mol around the peak by RMSD using the OC suite,[76] with RMSD cutoff as the global maximum in a histogram of pairwise RMSDs of all structures clustered. The centroid of the largest cluster is chosen as the representative structure of that state.

Interface contact maps.

In each simulation snapshot, we evaluate pairwise contacts between all residues in the simulation. We define two residues as being in contact if their C_β (C_α for glycine) are within 7.5 angstroms of each other. The count between every pair of residues is normalized for the total number of simulation snapshots.

Nuclear magnetic resonance structural analysis.

All NMR data were acquired on a Bruker Avance NEO 600 MHz instrument equipped with a triple resonance (1H, 13C, 15N) TCI cryoprobe. 1 mM peptide was dissolved in 500 μL of 20 mM phosphate buffer at pH 6.5 with 5% D_2O. The sample was then transferred to a 5 mM NMR tube. All NMR experiments were carried out on a Bruker 600 MHz instrument equipped with a triple resonance TCI cryoprobe at room temperature. 1H-1H TOCSY (with mixing time 75 ms) and NOESY (mixing times 400 ms and 600 ms) were acquired using excitation sculpting scheme for water suppression. The sample was then lyophilized and re-dissolved in 500 μL 99.9% D_2O. The same TOCSY and NOESY data were acquired in the D_2O sample. TOCSY data was used to assign residue types and the NOESY data in H_2O used for sequential assignment.

Electron microscopy.

Transmission electron micrographs of diluted samples were obtained using a Tecnai G2 Spirit BioTwin transmission electron microscope (FEI; Hillsboro, OR) with 80 kV accelerating voltage by a side-mounted Gatan Orius SC200 CCD camera. Fibrils imaged by TEM were prepared as follows. MAD1 was solubilized at 20 μM in phosphate buffer at either pH 4.5 or 7.4 and incubated at room temperature for 30 minutes. Then, 5 μL was deposited on a Formvar/carbon coated 400 mesh Cu grid and allowed to adsorb for 5 minutes. This solution was then wicked away and the grid was washed twice with buffer. In the same manner, 3 μL of 0.2 μm filtered 1% uranyl acetate was deposited on the sample as a negative stain to enhance image contrast and immediately wicked until dry.

Mtb was diluted to an OD_{600} of 0.01 and treated with MAD1 at 0.1x, 0.5x, 1x, and 5 x MIC, and incubated at 37°C for 30 minutes. Following treatment, cells were pelleted by centrifugation at 7000 rpm for 10 minutes at 4°C. After overnight pre-fixation with a 2.5%

glutaraldehyde, 0.1 M sodium cacodylate buffer, the bacterial cells were washed twice and then post-fixed with 1% osmium tetroxide for 2 hours. The fixed samples were subsequently washed twice with PBS and dehydrated for 15 minutes in each of a graded ethanol series (50, 70, 90, and 100%) along with for 10 minutes in both a mixture (1:1, v/v) of absolute ethanol and acetone, and absolute acetone. Subsequently, the samples were transferred to a mixture (1:1, v/v) of absolute acetone and epoxy resin for 30 minutes followed by pure epoxy resin for overnight at a constant temperature. Finally, the specimens were sectioned using an ultramicrotome (Leica EM UC6 Microtome; Wetzlar, Germany), double stained by uranyl acetate and lead citrate, and observed by TEM.

For scanning electron microscopy studies, bacterial samples were prepared as above and imaged with a Zeiss SIGMA VP-FESEM (Oberkochen, Germany) with a 10 kV landing voltage. Samples were prepared by pelleting MAD1-treated cells via centrifugation at 7000 rpm for 10 min. at 4°C and washed twice with PBS under similar conditions. After overnight pre-fixation with 2.5% glutaraldehyde and 0.1 M sodium cacodylate buffer, samples were washed thrice with PBS. The fixed samples were subsequently dehydrated for 5 minutes in each of a graded ethanol series (25, 50, 70, 85, 95, and 3×100%). Afterwards, the samples were transferred to a critical point dryer (Leica EM CPD300; Wetzlar, Germany), where they were subjected to slow CO_2 exchange during 14 addition cycles at 28°C and 1 bar. Finally, the specimens were mounted onto aluminum stubs with conductive tabs, sputter coated with 10 nm Au/Pd and observed by SEM.

Peptide binding assays.

MAD1-peptidoglycan binding kinetics were determined using surface plasmon resonance spectroscopy (SR7500DC, Reichert Analytical Instrument; Depew, NY) using a method previously reported,[77,78] with minor modification. A carboxyl-functionalized sensor chip was used to immobilize *S. aureus* derived peptidoglycan, and the running buffer was 10 mM phosphate. In a typical experiment the surface was activated with a solution of 0.05 g/mL EDC and 0.02 g/mL NHS for 10 minutes at 20 μL/min. For immobilization, 3 μg/mL peptidoglycan in 10mM phosphate buffer (pH = 7.4) was injected at 5 μL/min, followed by 1 mM ethanolamine at 10 μL/min to block unbound activated sites. A second activation, immobilization and blockage cycle was run with peptidoglycan at 10 μg/mL. The instrument was equilibrated with running buffer for 30 minutes before experiments. For binding analyses, MAD1 was flowed over the chip at 25 μL/min for 6 minutes, followed by running buffer to obtain the dissociation profile. The biosensor was regenerated between treatment conditions with 40 mM NaOH at 100 μL/min for 1 minute. Data was collected using SPR Autolink Software (Reichert Technologies) and plotted using Scrubber 2.0 (BioLogic Software). Concentration data were zeroed to baseline by subtracting the reference channel signal. Kinetic analysis was performed with a 1:1 biomolecular interaction model fit, which enables the association (k_a) and dissociation (k_d) constants to be determined and for the binding affinity (K_D) to be calculated.

Binding of MAD-1 and mycolic acid was assayed using a reported film production protocol, [79] with slight modification. In brief, 7.5x concentrated mycolic acid stock solutions were prepared by serial dilution of purified mycolic acid powder in chloroform:methanol (9:1).

Stock concentrations of 75, 375, 750, 3750 and 7500 μM corresponded to a 1x, 5x, 10x, 50x, and 100x mycolic acid-to-peptide molar ratio, respectively. To produce the mycolic acid film, 20 μL of the 7.5x stock was added to a 2.0 mL microcentrifuge tube and gently swirled to homogeneously coat the bottom surface of the reaction tube. Next, the reaction tube was incubated at 65°C to evaporate the organic solvent, leaving an opaque mycolic acid film. 150 μL of a 10 μM MAD-1 solution was gently added to each reaction tube without disturbing the film and incubated at 37°C for 30 minutes. Supernatant was removed following centrifugation at 10,000 × g for 5 minutes and 4°C. To quantify the amount of unbound peptide, 50 μL of the supernatant was added to 100 uL Coomassie Brilliant Blue solution and incubated for 15 minutes at room temperature to allow dye conversion. Absorbance at 595 nm was measured by a microplate reader for analysis. Two independent experiments with five internal replicates each were performed, for a total n = 10.

Membrane disruption.

1-N-phenylnaphthylamine (NPN; λ_{ex} = 350 nm, λ_{em} = 420 nm) uptake was assessed as described previously,[37] with slight modifications. *M. tuberculosis* (H37Ra) cultures were grown to an OD_{600} of 1.0, washed and diluted to a 4x OD_{600} of 0.2 in DPBS. Equal parts bacteria and 40 μM NPN were mixed and 50 μL of the mixture was plated in an opaque black 96 well plate. 50 μL of 2X peptide solution was added to the well at predetermined time points at n=5. Suspensions were treated with MAD1 at 0.1x, 0.5x, 1x, 2x and 5 x MIC, or 100 μM digitonin as a positive lytic control.[80] Following convergent incubation times, the entire plate was read via plate reader (BioTek Cytation 3; Winooski, VT). Results were normalized to relevant background controls. Experiment was repeated for a total n = 10.

Impedance spectroscopy.

The IS measurements were performed using HP Agilent 4192A LF impedance analyzer connected to a set of two interdigitated electrodes (IDE). The IDEs were fabricated using photolithography techniques with electrodeposition of nickel on a glass substrate, as detailed elsewhere.[38] For each experiment, 100 μL of the target solution is deposited over the sensor. A 30 mV AC voltage is applied between the IDEs and the frequency is swept from 2 kHz to 5 MHz. We studied three different sample conditions: baseline media, culture supernatants and cells transferred to an equal volume of fresh medium (OD_{600} = 0.1). In order to elucidate the effect of the peptide on Mtb cells, each condition is further split between peptide-treated and non-peptide-treated samples (negative control samples), for a total of six sample conditions. After testing of each solution, the sensor is rinsed with Milli-Q Ultrapure deionized (DI) water and blow-dried with clean, dry air for consistency. At each frequency, the impedance can be expressed as $Z = |Z|e^{j\theta}$, where $|Z|$ is the impedance magnitude and θ is the its angle. We have utilized changes in $|Z|$ as the basis for these analyses, as calculated by $\Delta Z = 100 * (|Z| - [|Z|]_{baseline})/[|Z|]_{baseline}$. Three droplets were analyzed, and one droplet was analyzed thrice, for an n of 5 for each condition, to ensure inter- and intra-droplet consistency.

Membrane localization.

Mtb was diluted to an OD_{600} of 0.001 in PBS and treated with MAD1 at the MIC with 10% FITC-MAD1 doped in. Treated bacteria were incubated at 37°C while shaking before centrifugation and heat fixation on a glass slide. Cells were exposed to peptide for 15 minutes before fixation. Samples were imaged via confocal fluorescence microscopy. In parallel, cells were exposed to MAD1 for 45 minutes under the same protocol. In addition, propidium iodide (PI) was added at the time of treatment to analyze membrane integrity.

Polymicrobial assays.

Mtb, *S. aureus*, and *K. pneumoniae* were each back diluted to an OD_{600} of 0.004 in 7H9 broth and mixed in equal volumes. Polymicrobial cultures were then treated with MAD1 at various concentrations relative to the MIC of the peptide against Mtb. Treatment, or media control, was added to a final total bacterial OD_{600} of 0.003. The co-culture was incubated for an hour, pelleted by centrifugation at 7000 rpm for 10 minutes at 4°C and washed four times in PBS and resolubilized in 10% of the original volume. 100 μL were dried and fixed on a glass slide, before staining with auramine-rhodamine following manufacturer's instructions (Thermo Scientific Remel, Waltham, MA). Samples were imaged using an Olympus IX73 microscope (Tokyo, Japan). Three images each were taken of 3 samples and analyzed by ImageJ software. 15 cells per image were analyzed (n = 135) for cellular fluorescence, with standard error reported.

In parallel, peptide cytotoxicity curves are generated for each of the tested species (mycobacteria, Gram-positive and Gram-negative). Treatment was performed in the same manner described for MIC assays. Mtb plates were grown for 7 days to reach an adequate OD_{600}. Following incubation, wells are thoroughly mixed via pipette and transferred to a flat bottom plate for optical density measurements. Treatments were performed with n > 3. Curve fitting was performed using GraphPad Prism software as a nonlinear regression of semi log data.

For growth inhibition studies, cultures at an OD_{600} of 0.001 were treated with MAD1 at 4 x MIC_{Mtb} and growth monitored via OD_{600} measurements over time. Untreated cultures were monitored as controls.[81] OD_{600} measurements for Mtb were taken every 3 days, while *S. aureus* and *K. pneumoniae* were monitored every 2–4 hours until cultures reached stationary phase. The resulting data were analyzed using nonlinear sigmoidal regression as performed by GraphPad Prism. All curves were performed at n = 12 and include at least 2 genetic populations.

Cell toxicity.

NL20, HUVEC, and RAW 264.7 were plated in tissue-treated 96-well plates at 5×10^3 cells/well and allowed to adhere overnight. THP-1 monocytes were plated at 1.5×10^4 cells/well in a 96-well plate and incubated for 72 hours in media supplemented with 200 nM PMA to induce differentiation into naive M0 macrophages, as previously described.[82] Following differentiation, THP-1 cells were incubated overnight in PMA-free media. All cells were treated for 24 hours with serial dilutions of MAD1. Cells treated with blank media or 20% DMSO served as negative and positive controls, respectively. After treatment, cells were

washed with blank media before addition of 100 μL MTT solution (0.5 mg/mL) and incubated for 2 hours. Supernatant was removed and the cell impermeable formazan product was solubilized by the addition of 100 μL DMSO and absorbance read with a microplate reader at 540 nm. Percent viability was calculated with the following equation: $\left(Abs_{treatment} - Abs_{pos}\right)/\left(Abs_{neg} - Abs_{pos}\right) \times 100\%$. The resulting data were analyzed using nonlinear regression of semi log data as performed by GraphPad Prism. All curves were performed at n = 12 and include at least 2 genetic populations.

Intracellular killing assay.

Clearance of infected macrophages was analyzed as described previously.[83–85] Briefly, RAW 264.7 cells were seeded in a cell culture treated 96 well plate at 1.5×10^4 cells/well. Adhered macrophages were infected with Mtb (MOI of 10) for 5 hours. Remaining extracellular bacteria were removed by washing thrice with DPBS. Infected macrophages were treated with MAD1 from 0.5 – 10 x MIC and incubated for 24 hours. Due to the altered macrophage density and reliance on internalization, MIC referenced concentrations were not adjusted to bacterial density and were instead based on MIC = 2.5 μM. Intracellular bacteria were isolated by trypsinizing the macrophages for 10 minutes at 37°C and scraping followed by centrifugation at 4600 × g for 10 minutes. Each sample was then resuspended, serially diluted and plated on 7H9 agar. Colonies were counted 24 days later. The experiment was repeated with 3 internal replicates for a total n = 6.

Combinatorial drug screening for synergy.

Checkerboard assays were performed by preparing 2-fold, 4x serial dilutions of the peptide in media and added to a 96-well microtiter plate. 2-fold, 4x serial dilutions of each TB antibiotic was prepared in a separate 96-well microtiter plate in an orthogonal direction to the peptide. The antibiotic dilutions were then added to their respective rows in the plate of diluted peptide in a 1:1 volume ratio. As with MIC assays, 50 μL of bacterial solutions at an OD_{600} of 0.002 were added to all wells for a final assay volume of 100 μL. The plate was sealed and incubated at 37°C for 4 days before growth determined via visual inspection.[86]

Statistical Analysis.

Statistical significance was determined by performing a two-tailed, unpaired student's t-test using GraphPad Prism software, unless stated otherwise. A confidence level of 95% (α = 0.05) was used. Significance denoted in figures is * $p < 0.001$, unless exact p value is given.

Reporting summary.

Further information on research design is available in the Nature Research Reporting Summary linked to this article.

Supplementary Material

Refer to Web version on PubMed Central for supplementary material.

Acknowledgements

We acknowledge and thank the Penn State Microscopy and Cytometry Facility – University Park, PA for assistance with confocal and electron microscopy. We also acknowledge the Penn State X-Ray Crystallography Facility – University Park, PA for use of the CD spectrophotometer. We also acknowledge the Penn State NMR Facility – University Park, PA for use of NMR instrumentation. Funding for this research was provided by the Penn State Institute of Energy and the Environment Human Health and the Environment Seed Grant awarded to S.H.M. This work was also supported by NIH grant number AI123146 to A.D.B. A. W. S was supported by funds from the Penn State Graduate Research Fellowship.

Data availability

The main data supporting the results in this study are available within the paper and its Supplementary Information. The raw and analysed datasets generated during the study are too large to be publicly shared, yet they are available for research purposes from the corresponding authors on reasonable request.

References

1. Blaser MJ Antibiotic use and its consequences for the normal microbiome. Science 352, 544–545 (2016). [PubMed: 27126037]
2. Brito IL et al. Mobile genes in the human microbiome are structured from global to individual scales. Nature 535, 435–439 (2016). [PubMed: 27409808]
3. Smillie CS et al. Ecology drives a global network of gene exchange connecting the human microbiome. Nature 480, 241 (2011). [PubMed: 22037308]
4. Levy M, Blacher E & Elinav E Microbiome, metabolites and host immunity. Curr. Opin. Microbiol 35, 8–15 (2017). [PubMed: 27883933]
5. Levy M, Kolodziejczyk AA, Thaiss CA & Elinav E Dysbiosis and the immune system. Nat. Rev. Immunol 17, 219 (2017). [PubMed: 28260787]
6. Spellberg B & Rex JH The value of single-pathogen antibacterial agents. Nat. Rev. Drug Discovery 12, 963–963, 10.1038/nrd3957-c1 (2013). [PubMed: 24232373]
7. Lewis K Recover the lost art of drug discovery. Nature 485, 439–440, 10.1038/485439a (2012). [PubMed: 22622552]
8. Maxson T & Mitchell DA Targeted Treatment for Bacterial Infections: Prospects for Pathogen-Specific Antibiotics Coupled with Rapid Diagnostics. Tetrahedron 72, 3609–3624, 10.1016/j.tet.2015.09.069 (2016). [PubMed: 27429480]
9. Brown ED & Wright GD Antibacterial drug discovery in the resistance era. Nature 529, 336–343 (2016). [PubMed: 26791724]
10. Melander RJ, Zurawski DV & Melander C Narrow-Spectrum Antibacterial Agents. Medchemcomm 9, 12–21 (2018). [PubMed: 29527285]
11. Niederweis M Mycobacterial porins – new channel proteins in unique outer membranes. Mol. Microbiol 49, 1167–1177 (2003). [PubMed: 12940978]
12. Mahfoud M, Sukumaran S, Hülsmann P, Grieger K & Niederweis M Topology of the porin MspA in the outer membrane of Mycobacterium smegmatis. J. Biol. Chem 281, 5908–5915 (2006). [PubMed: 16352610]
13. Alderwick LJ, Harrison J, Lloyd GS & Birch HL The Mycobacterial Cell Wall—Peptidoglycan and Arabinogalactan. Cold Spring Harbor Perspect. Med 5 (2015).
14. Tossi A, Sandri L & Giangaspero A Amphipathic, α-helical antimicrobial peptides. Peptide Science 55, 4–30 (2000). [PubMed: 10931439]
15. Huang Y, Huang J & Chen Y Alpha-helical cationic antimicrobial peptides: relationships of structure and function. Protein & cell 1, 143–152 (2010). [PubMed: 21203984]
16. Sharpe HJ, Stevens TJ & Munro S A comprehensive comparison of transmembrane domains reveals organelle-specific properties. Cell 142, 158–169 (2010). [PubMed: 20603021]

17. Wang Q et al. PE/PPE proteins mediate nutrient transport across the outer membrane of Mycobacterium tuberculosis. Science 367, 1147–1151 (2020). [PubMed: 32139546]
18. Melly G & Purdy GE MmpL Proteins in Physiology and Pathogenesis of M. tuberculosis. Microorganisms 7, 70, 10.3390/microorganisms7030070 (2019).
19. Vandal OH, Pierini LM, Schnappinger D, Nathan CF & Ehrt S A membrane protein preserves intrabacterial pH in intraphagosomal Mycobacterium tuberculosis. Nat. Med 14, 849–854 (2008). [PubMed: 18641659]
20. Vergne I et al. Mechanism of phagolysosome biogenesis block by viable Mycobacterium tuberculosis. Proc. Natl. Acad. Sci 102, 4033–4038 (2005). [PubMed: 15753315]
21. Deretic V et al. Mycobacterium tuberculosis inhibition of phagolysosome biogenesis and autophagy as a host defence mechanism. Cell. Microbiol 8, 719–727 (2006). [PubMed: 16611222]
22. Cochran AG, Skelton NJ & Starovasnik MA Tryptophan zippers: Stable, monomeric β-hairpins. Proc. Natl. Acad. Sci 98, 5578–5583 (2001). [PubMed: 11331745]
23. Liu J, Yong W, Deng Y, Kallenbach NR & Lu M Atomic structure of a tryptophan-zipper pentamer. Proc. Natl. Acad. Sci 101, 16156–16161 (2004). [PubMed: 15520380]
24. Liu J, Yong W, Deng Y, Kallenbach NR & Lu M Atomic structure of a tryptophan-zipper pentamer. Proc. Natl. Acad. Sci 101, 16156–16161 (2004). [PubMed: 15520380]
25. Heinz C, Karosi S & Niederweis M High-level expression of the mycobacterial porin MspA in Escherichia coli and purification of the recombinant protein. J. Chromatogr. B: Biomed. Sci. Appl 790, 337–348 (2003).
26. Ragazzon G & Prins LJ Energy consumption in chemical fuel-driven self-assembly. Nat. Nanotechnol 13, 882–889 (2018). [PubMed: 30224796]
27. Lin Y et al. Residue-Specific Solvation-Directed Thermodynamic and Kinetic Control over Peptide Self-Assembly with 1D/2D Structure Selection. ACS Nano 13, 1900–1909 (2019). [PubMed: 30673202]
28. Vandal OH, Nathan CF & Ehrt S Acid resistance in Mycobacterium tuberculosis. J. Bacteriol 191, 4714–4721 (2009). [PubMed: 19465648]
29. The European Committee on Antimicrobial Susceptibility Testing (2018).
30. Ramón-García S et al. Targeting Mycobacterium tuberculosis and Other Microbial Pathogens Using Improved Synthetic Antibacterial Peptides. Antimicrob. Agents Chemother 57, 2295–2303 (2013). [PubMed: 23478953]
31. Brown L, Wolf JM, Prados-Rosales R & Casadevall A Through the wall: extracellular vesicles in Gram-positive bacteria, mycobacteria and fungi. Nat. Rev. Microbiol 13, 620–630 (2015). [PubMed: 26324094]
32. Maitra A et al. Cell wall peptidoglycan in Mycobacterium tuberculosis: An Achilles' heel for the TB-causing pathogen. FEMS Microbiol. Rev 43, 548–575 (2019). [PubMed: 31183501]
33. Muheim C et al. Increasing the permeability of Escherichia coli using MAC13243. Sci. Rep 7, 17629 (2017). [PubMed: 29247166]
34. Helander I & Mattila-Sandholm T Fluorometric assessment of Gram-negative bacterial permeabilization. J. Appl. Microbiol 88, 213–219 (2000). [PubMed: 10735988]
35. Eriksson M, Nielsen PE & Good L Cell permeabilization and uptake of antisense peptide-peptide nucleic acid (PNA) into Escherichia coli. J. Biol. Chem 277, 7144–7147 (2002). [PubMed: 11739379]
36. Halder S et al. Alteration of Zeta potential and membrane permeability in bacteria: a study with cationic agents. Springerplus 4, 672–672 (2015). [PubMed: 26558175]
37. Yavvari PS et al. Clathrin-Independent Killing of Intracellular Mycobacteria and Biofilm Disruptions Using Synthetic Antimicrobial Polymers. Biomacromolecules 18, 2024–2033 (2017). [PubMed: 28561567]
38. Butler D, Goel N, Goodnight L, Tadigadapa S & Ebrahimi A Detection of bacterial metabolism in lag-phase using impedance spectroscopy of agar-integrated 3D microelectrodes. Biosens. Bioelectron 129, 269–276 (2019). [PubMed: 30297173]
39. Bolotsky A et al. Two-Dimensional Materials in Biosensing and Healthcare: From In Vitro Diagnostics to Optogenetics and Beyond. ACS Nano 13, 9781–9810 (2019). [PubMed: 31430131]

40. Inoue S et al. Dielectrophoretic characterization of antibiotic-treated Mycobacterium tuberculosis complex cells. Anal. Bioanal. Chem 407, 7673–7680 (2015). [PubMed: 26231690]
41. Perera AS, Wang H, Shrestha TB, Troyer DL & Bossmann SH Nanoscopic surfactant behavior of the porin MspA in aqueous media. Beilstein J. Nanotechnol 4, 278–284 (2013). [PubMed: 23766950]
42. Hu B et al. Polyphenol-Binding Amyloid Fibrils Self-Assemble into Reversible Hydrogels with Antibacterial Activity. ACS Nano 12, 3385–3396 (2018). [PubMed: 29553709]
43. Torrent M, Pulido D, Nogués MV & Boix E Exploring New Biological Functions of Amyloids: Bacteria Cell Agglutination Mediated by Host Protein Aggregation. PLOS Pathogens 8, e1003005, 10.1371/journal.ppat.1003005 (2012). [PubMed: 23133388]
44. Truant J, Brett W & Thomas W Jr Fluorescence microscopy of tubercle bacilli stained with auramine and rhodamine. Henry Ford Hosp. Med. J 10, 287–296 (1962). [PubMed: 13922644]
45. Danilchanka O, Pavlenok M & Niederweis M Role of Porins for Uptake of Antibiotics by Mycobacterium smegmatis. Antimicrob. Agents Chemother 52, 3127–3134 (2008). [PubMed: 18559650]
46. Chairatana P & Nolan EM Molecular basis for self-assembly of a human host-defense peptide that entraps bacterial pathogens. J. Am. Chem. Soc 136, 13267–13276 (2014). [PubMed: 25158166]
47. Chairatana P & Nolan EM Human α-defensin 6: a small peptide that self-assembles and protects the host by entangling microbes. Acc. Chem. Res 50, 960–967 (2017). [PubMed: 28296382]
48. Schroeder B et al. Paneth cell α-defensin 6 (HD-6) is an antimicrobial peptide. Mucosal immunology 8, 661–671 (2015). [PubMed: 25354318]
49. Vetterli SU et al. Thanatin targets the intermembrane protein complex required for lipopolysaccharide transport in Escherichia coli. Science Advances 4, eaau2634, 10.1126/sciadv.aau2634 (2018). [PubMed: 30443594]
50. Robinson JA Folded Synthetic Peptides and Other Molecules Targeting Outer Membrane Protein Complexes in Gram-Negative Bacteria. Front Chem 7, 45–45, 10.3389/fchem.2019.00045 (2019). [PubMed: 30788339]
51. Luther A et al. Chimeric peptidomimetic antibiotics against Gram-negative bacteria. Nature 576, 452–458, 10.1038/s41586-019-1665-6 (2019). [PubMed: 31645764]
52. Levitt M Conformational preferences of amino acids in globular proteins. Biochemistry 17, 4277–4285 (1978). [PubMed: 708713]
53. Gehman JD et al. Effect of Antimicrobial Peptides from Australian Tree Frogs on Anionic Phospholipid Membranes. Biochemistry 47, 8557–8565 (2008). [PubMed: 18652483]
54. Jiang Z et al. Effects of net charge and the number of positively charged residues on the biological activity of amphipathic alpha-helical cationic antimicrobial peptides. Biopolymers 90, 369–383 (2008). [PubMed: 18098173]
55. Mikut R et al. Improving short antimicrobial peptides despite elusive rules for activity. Biochim. Biophys. Acta, Biomembr 1858, 1024–1033 (2016).
56. Rekdal Ø et al. Relative spatial positions of tryptophan and cationic residues in helical membrane-active peptides determine their cytotoxicity. J. Biol. Chem 287, 233–244 (2012). [PubMed: 22057278]
57. Medina SH et al. An Intrinsically Disordered Peptide Facilitates Non-Endosomal Cell Entry. Angew. Chem., Int. Ed 55, 3369–3372 (2016).
58. Rath P et al. Cord factor (trehalose 6,6′-dimycolate) forms fully stable and non-permeable lipid bilayers required for a functional outer membrane. Biochim. Biophys. Acta, Rev. Biomembr 1828, 2173–2181 (2013).
59. Epand RF, Savage PB & Epand RM Bacterial lipid composition and the antimicrobial efficacy of cationic steroid compounds (Ceragenins). Biochim. Biophys. Acta, Biomembr 1768, 2500–2509 (2007).
60. Lombardi L et al. Antimicrobial peptides at work: interaction of myxinidin and its mutant WMR with lipid bilayers mimicking the P. aeruginosa and E. coli membranes. Sci. Rep 7, 44425–44425 (2017). [PubMed: 28294185]
61. Zehethofer N et al. Lipid Analysis of Airway Epithelial Cells for Studying Respiratory Diseases. Chromatographia 78, 403–413 (2015). [PubMed: 25750457]

62. Andrews JM Determination of minimum inhibitory concentrations. J. Antimicrob. Chemother 48, 5–16 (2001). [PubMed: 11420333]
63. Zhang Y, Zhang H & Sun Z Susceptibility of Mycobacterium tuberculosis to weak acids. J. Antimicrob. Chemother 52, 56–60 (2003). [PubMed: 12775670]
64. Avitabile C, D'Andrea LD & Romanelli A Circular Dichroism studies on the interactions of antimicrobial peptides with bacterial cells. Sci. Rep 4, 4293–4293 (2014). [PubMed: 24618744]
65. Tao L et al. Probing the Amyloid Peptide-Membrane Interaction Using a Liposome Model System. J. Self-Assem. Mol. Electron 4, 1–18 (2016).
66. Dokholyan NV, Buldyrev SV, Stanley HE & Shakhnovich EI Discrete molecular dynamics studies of the folding of a protein-like model. Folding Des 3, 577–587 (1998).
67. Proctor EA, Ding F & Dokholyan NV Discrete molecular dynamics. Wiley Interdiscip. Rev.: Comput. Mol. Sci 1, 80–92 (2011).
68. Ding F, Tsao D, Nie H & Dokholyan NV Ab initio folding of proteins with all-atom discrete molecular dynamics. Structure 16, 1010–1018 (2008). [PubMed: 18611374]
69. Ding F & Dokholyan NV Emergence of protein fold families through rational design. PLoS Comput. Biol 2, e85 (2006). [PubMed: 16839198]
70. Lazaridis T & Karplus M Effective energy function for proteins in solution. Proteins: Struct., Funct., Bioinf 35, 133–152 (1999).
71. Ding F, Borreguero JM, Buldyrey SV, Stanley HE & Dokholyan NV Mechanism for the α-helix to β-hairpin transition. Proteins: Struct., Funct., Bioinf 53, 220–228 (2003).
72. Sugita Y & Okamoto Y Replica-exchange molecular dynamics method for protein folding. Chem. Phys. Lett 314, 141–151 (1999).
73. Okamoto Y Generalized-ensemble algorithms: enhanced sampling techniques for Monte Carlo and molecular dynamics simulations. J. Mol. Graphics Modell 22, 425–439 (2004).
74. Feig M, Karanicolas J & Brooks CL III MMTSB Tool Set: enhanced sampling and multiscale modeling methods for applications in structural biology. J. Mol. Graphics Modell 22, 377–395 (2004).
75. Kumar S, Rosenberg JM, Bouzida D, Swendsen RH & Kollman PA The weighted histogram analysis method for free-energy calculations on biomolecules. I. The method. J. Comput. Chem 13, 1011–1021 (1992).
76. Barton G OC-A cluster analysis program University of Dundee, Scotland, UK (2002).
77. Coyne J, Davis B, Kauffman D, Zhao N & Wang Y Polymer Microneedle Mediated Local Aptamer Delivery for Blocking the Function of Vascular Endothelial Growth Factor. ACS Biomater. Sci. Eng 3, 3395–3403 (2017). [PubMed: 29707631]
78. Burch JM, Mashayekh S, Wykoff DD & Grimes CL Bacterial Derived Carbohydrates Bind Cyr1 and Trigger Hyphal Growth in Candida albicans. ACS Infect. Dis 4, 53–58 (2018). [PubMed: 29040806]
79. Date T, Sekine J, Matsuno H & Serizawa T Polymer-binding peptides for the noncovalent modification of polymer surfaces: effects of peptide density on the subsequent immobilization of functional proteins. ACS Appl. Mater. Interfaces 3, 351–359 (2011). [PubMed: 21288050]
80. Sudji IR, Subburaj Y, Frenkel N, García-Sáez AJ & Wink M Membrane disintegration caused by the steroid saponin digitonin is related to the presence of cholesterol. Molecules 20, 20146–20160 (2015). [PubMed: 26569199]
81. Bishop JG, Schanbacher F, Ferguson LC & Smith KL In vitro growth inhibition of mastitis-causing coliform bacteria by bovine apo-lactoferrin and reversal of inhibition by citrate and high concentrations of apo-lactoferin. Infect. Immun 14, 911–918 (1976). [PubMed: 791866]
82. Xie Z et al. Immune Cell-Mediated Biodegradable Theranostic Nanoparticles for Melanoma Targeting and Drug Delivery. Small 13, 1603121 (2017).
83. Singh B, Saqib M, Gupta A, Kumar P & Bhaskar S Autophagy induction by Mycobacterium indicus pranii promotes Mycobacterium tuberculosis clearance from RAW 264.7 macrophages. PloS One 12, e0189606 (2017). [PubMed: 29236768]
84. Iyoda T et al. A novel mechanism underlying the basic defensive response of macrophages against Mycobacterium infection. J. Immunol 192, 4254–4262 (2014). [PubMed: 24663676]

85. Jo SH et al. Calreticulin modulates the intracellular survival of mycobacteria by regulating ER-stress-mediated apoptosis. Oncotarget 8, 58686 (2017). [PubMed: 28938588]

86. Xu X et al. Synergistic combination of two antimicrobial agents closing each other's mutant selection windows to prevent antimicrobial resistance. Sci. Rep 8, 1–7 (2018). [PubMed: 29311619]

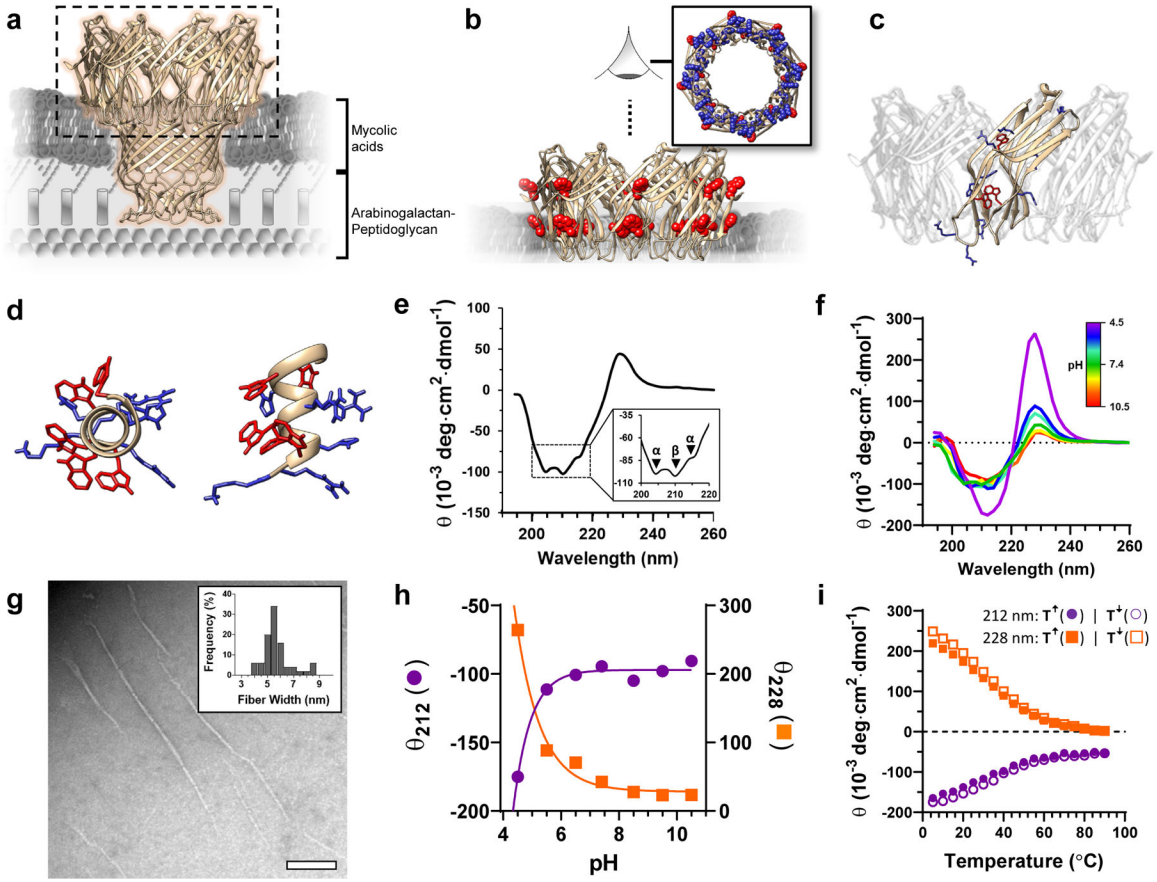

Fig. 1 |. Biomimetic design and biophysical analysis of MAD1.

a, Model of the MspA porin docked in a rendering of the mycobacterial cell envelope (PDB structure 1UUN). **b**, Concentric rings of tryptophan residues (red) circumscribing the porin head is key to MspA's ability to anchor at the mycolipid-water interface. *Inset:* Model of MspA viewed from above (red = tryptophan, blue = basic residues). **c**, Highlighted protein sub-unit of the MspA rim domain. **d**, Minimized model of a MAD1 helix (*left*: axial view; r*ight*: side view; red = tryptophan, blue = basic residues). The peptide mimics the facially amphiphilic character and extended terminal basic residues of the MspA rim subunit. **e**, **f**, Circular dichroism spectra of MAD1 at (**e**) physiologic pH (7.4; inset magnifies signal from 200 – 220 nm) or (**f**) as a function of decreasing pH from 10.5 (red) to 4.5 (purple). **g**, TEM micrograph of MAD1 nanofibrillar assembles (pH 4.5). Scale bar = 100 nm. Representative micrograph shown from three independent experiments with similar results. Two additional images from replicate experiments are shown in Supplementary Fig. 4. *Inset:* Histogram of lateral fibril width (n = 50). **h**, pH-dependent change in the molar ellipticity of MAD1 at 212nm (●, purple) or 228nm (■, orange). **i**, Temperature-dependent change in MAD1 molar ellipticity at 212nm (●, purple) or 228nm (■, orange). Closed symbols represent temperature ramp up, and open symbols the reverse temperature ramp down, of n = 3 technical replicates.

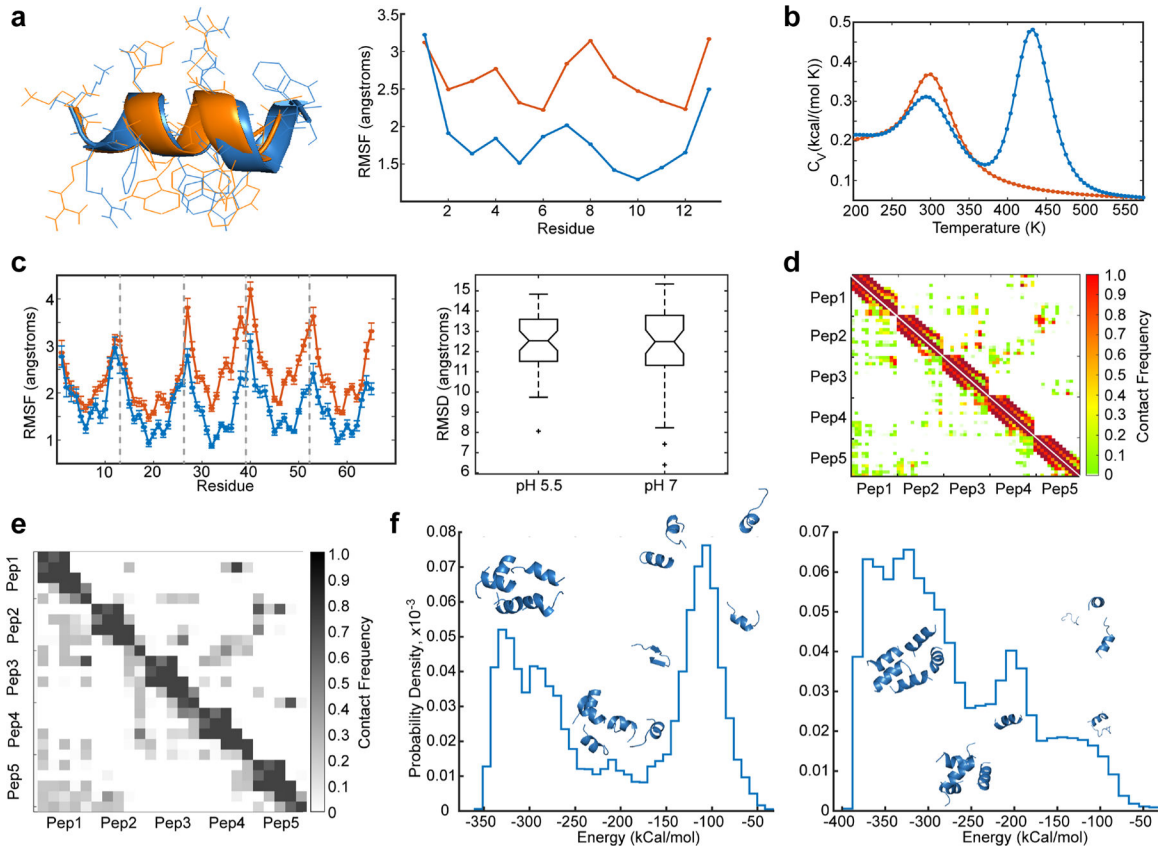

Fig. 2 |. Atomistic mechanisms of MAD1 assembly.

a, Structure (*left*) of the MAD1 peptide at pH 7 (blue) and pH 5.5 (orange), and profile of MAD1 dynamics as root mean square fluctuations at each residue over simulation at equilibrium (*right*). **b,** Volume-constant specific heat of MAD1 monomer at pH 7 (blue) and pH 5.5 (orange). **c,** Root mean square fluctuations (*left*) at each residue of MAD1 pentameric assembly. Data shown are mean ± S.E.M. over 10 independent simulations. Vertical dashed lines separate individual monomers. As expected, we note peaks of increased fluctuation at peptide N- and C-termini. Box-whisker plot (*right*) of pairwise root mean square deviation comparison between consensus structures of 10 randomized simulation iterations of MAD1 pentameric assembly (45 comparisons total for each pH). The box bounds the interquartile range (acid: [11.51 Å – 13.60 Å], neutral: [11.32 Å – 13.79 Å]), with centerline being the median (acid: 12.54 Å, neutral: 12.49 Å). Whiskers extend to the adjacent values that lie within 1.5 x interquartile range beyond the box. Points lying outside the whiskers are outliers. **d,** Heat map of residue-residue contact frequencies in MAD1 pentamer assembly at pH 7 (*upper diagonal*) and pH 5.5 (*lower diagonal*). **e,** Heat map of tryptophan-tryptophan contact frequencies in MAD1 pentamer assembly at pH 7 (*upper diagonal*) and pH 5.5 (*lower diagonal*). **f,** Normalized histogram of potential energies of structures occurring at energetic transition at pH 5.5 (*left*) and pH 7 (*right*). Peaks represent discrete energetic transition states, with representative structures of each energetic state pictured over each peak.

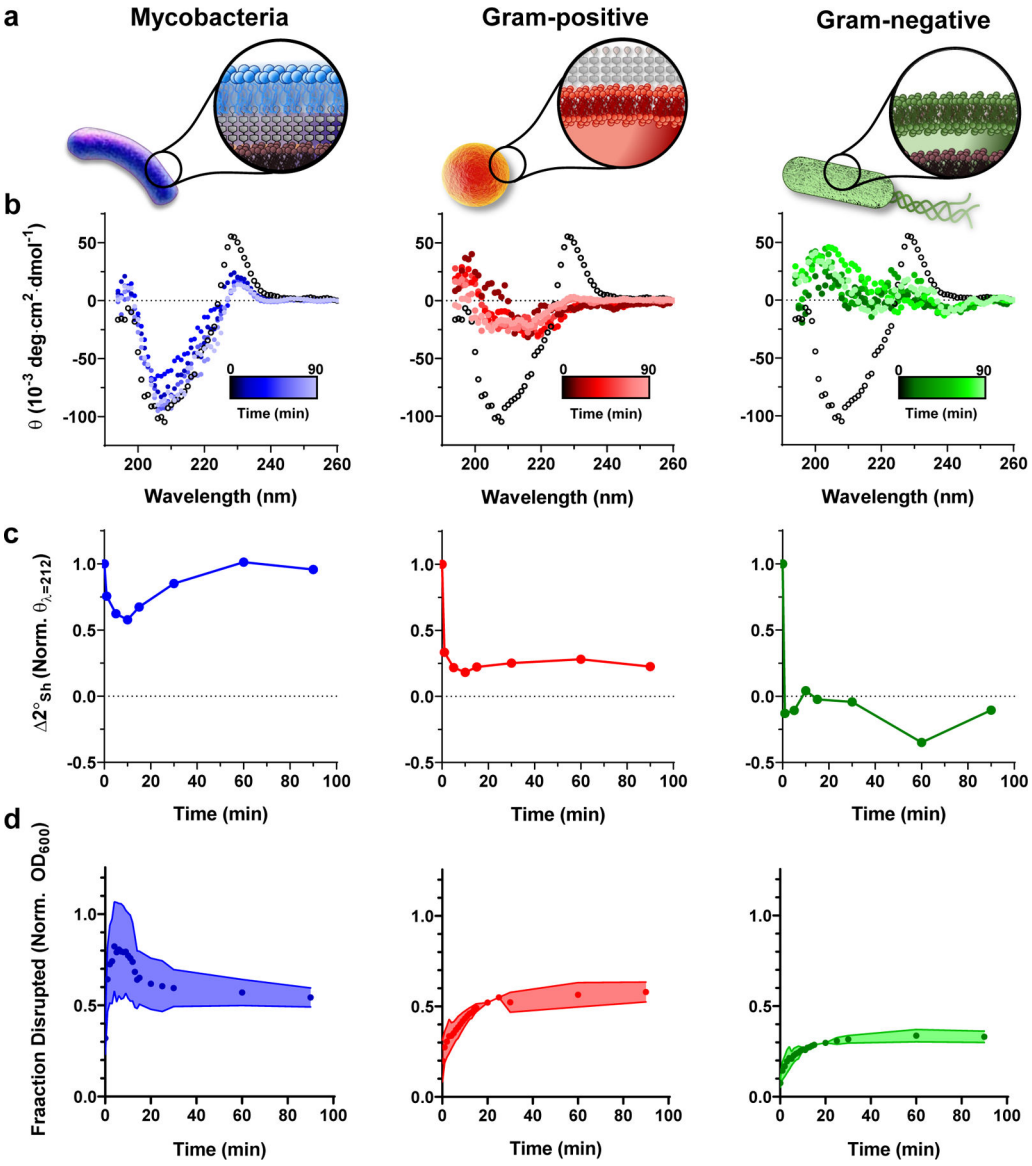

Fig. 3 |. *Ex cellulo* analysis of MAD1 myco-membrane specificity.

a, Schematic of mycobacterial, Gram-positive and Gram-negative outer membrane structures. **b**, CD spectrum of MAD1 in the presence of model liposomal membrane analogues. Peptide spectra at t = 0 represented in open black circles, and t → 90 min. shown as increasing lighter shades of color. **c**, Magnitude change in MAD1 β-sheet secondary structure ($\Delta 2°_{sh}$) over time, derived from CD spectra shown in panel a. Dotted line demarcates complete loss of sheet-rich architectures. **d**, Fractional disruption of model microbial membranes determined by optical density (OD_{600}) at 20 μM MAD1. Measurements normalized to unextruded lipids as a positive control. Symbols represent mean value; shaded regions report S.E.M. Statistical significance of final OD_{600} measurement (90 min.) for myco-membrane data (blue) determined using a two-tailed Student's t-test relative to peak disruption (4 min.). n ≥ 3 for all experiments, with representative CD spectra shown.

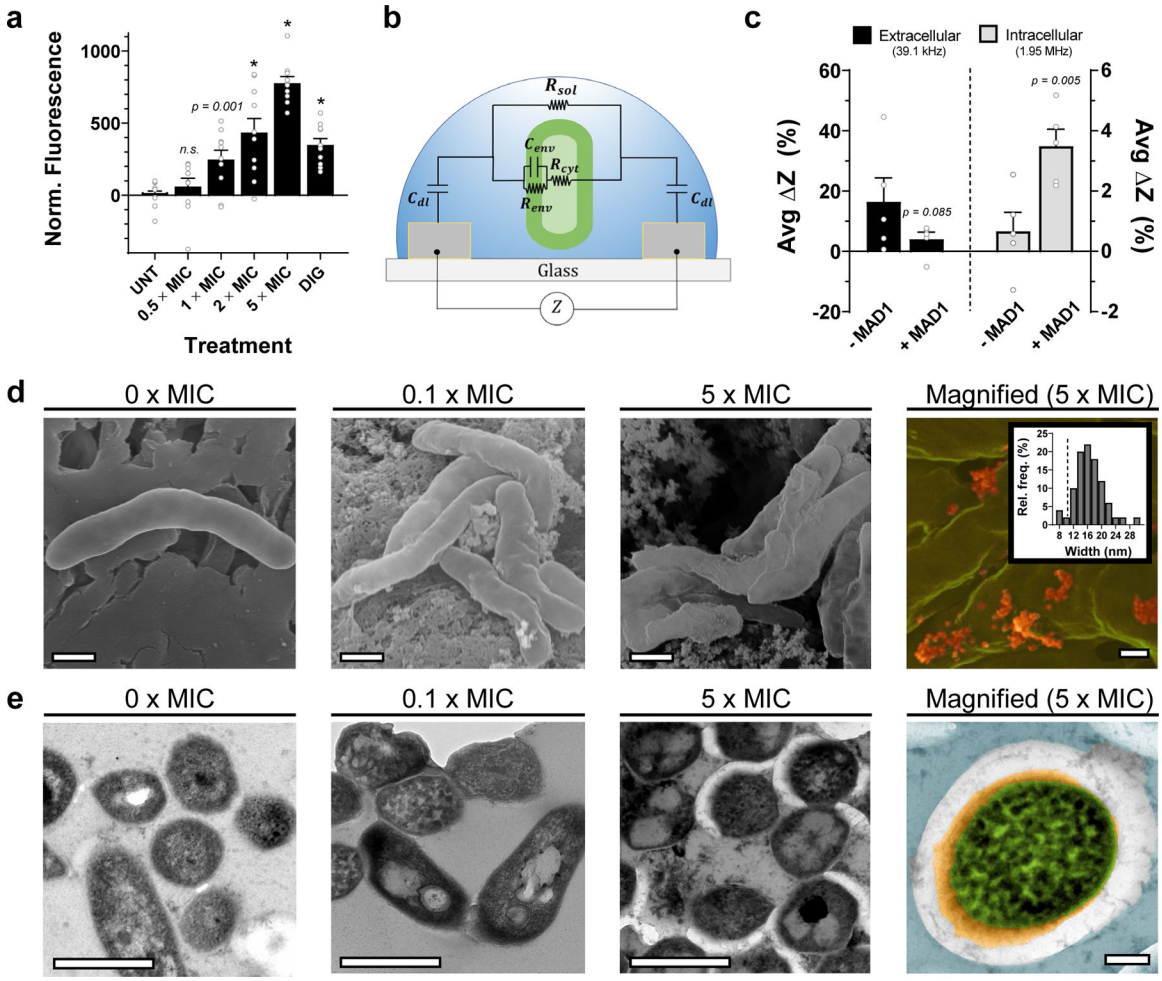

Fig. 4 |. *In situ* characterization of Mtb envelope disruption by MAD1.

a, Relative membrane integrity of Mtb after a 45 min. incubation in the absence (untreated, UNT) or presence (x MIC) of increasing MAD1 concentrations, as determined by NPN fluorescence. Digitonin (DIG) included as a positive lytic control. Bars represent mean ± S.E.M., with individual data points overlayed (n = 10 biologically independent samples across two independent experiments). Statistical significance determined using a one-tailed Student's t-test relative to untreated control, with p values reported or * indicating $p < 0.001$. n.s. = not statistically significant. **b**, Circuit diagram utilized to model system impedance for IS experiments. Total impedance is comprised of solution resistance (R_{sol}), cell envelope resistance (R_{env}), cell envelope capacitance (C_{env}), cytoplasmic resistance (R_{cyt}), and double-layer capacitance (C_{dl}). **c**, *Left*: Percent change of solution impedance (ΔZ @ 39.1 kHz) in the absence (Mtb) or presence (Mtb + MAD1) of MAD1 at 1 x MIC. In the absence of cells, total impedance is dominated by R_{sol} and C_{dl}. *Right*: Percent change in cell envelope impedance (ΔZ @ 1.95 MHz) in the absence or presence of MAD1 at 1 x MIC. Processed impedance spectra, and associated raw data, are shown in Supplementary Figs. 11 and 12, respectively. Individual data points shown as open circles (n = 5, representing three biologically independent samples), and bars represent mean ± S.E.M. Statistical significance

determined relative to untreated control, with p values reported from a one-tailed Student's t-test. **d**, SEM and **e**, TEM micrographs of Mtb cells before (0 x MIC) and after treatment with MAD1 at 0.1 x or 5 x MIC. Scale bar = 0.5 μm. *Right*: Magnified and false-colored EM images of the Mtb (**d**) outer surface (green = Mtb cell envelope, red = MAD1 supramolecular structures) and (**e**) cellular cross-section following treatment with 5 x MIC MAD1 (green = Mtb cytoplasm, yellow = intracellular leakage, white space = delaminated cell wall). *Panel d inset*: histogram of MAD1 cylindrical assembly width (n = 50); dashed line shows the reported diameter of the MspA porin. Scale bar = 100 nm. Representative micrographs in panels d and e are taken from three independent experiments, with similar results. Additional SEM and TEM images from replicate experiments are shown in Supplementary Figures 14 and 17, respectively.

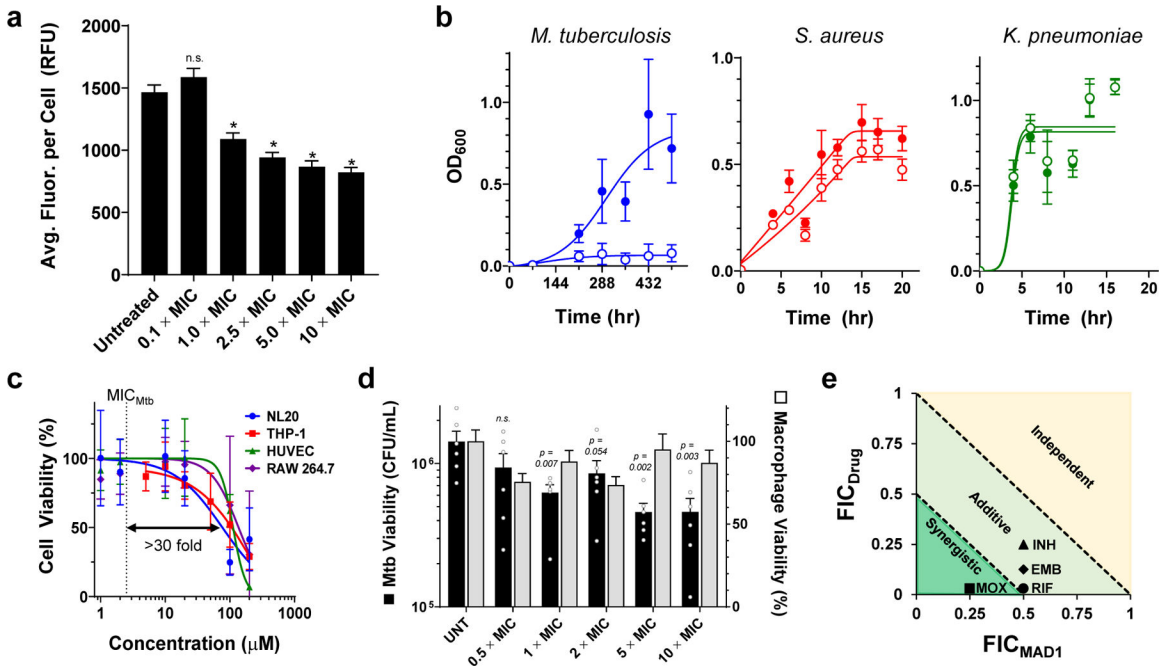

Fig. 5 |. MAD1 polymicrobial selectivity and combinatorial synergy.

a, Relative membrane integrity of Mtb cells in the absence (untreated) or presence (x MIC) of increasing MAD1 concentrations. Membrane disruption quantified by auramine-rhodamine staining in a polymicrobial co-culture of Mtb with *S. aureus* and *K. pneumoniae*. Bars represent mean ± S.E.M. and statistical significance determined via a two-tailed Student's t-test relative to untreated control, with * indicating $p < 0.001$ (n = 135 cells measured across three independent experiments). n.s. = not statistically significant. **b,** Polymicrobial growth curves monitoring the proliferation of each bacterial strain in the absence (●) or presence (○) of MAD1 at 4 × MIC_{Mtb}, shown as mean ± S.D. with n = 12 biologically independent samples across two independent experiments. **c,** Cytotoxicity of MAD1 against pathophysiologically relevant mammalian cell lines, including human normal lung epithelium (NL20), human monocytes (THP-1), murine macrophages (RAW 264.7; n = 36 biologically independent samples across three independent experiments), and vascular endothelial cells (HUVEC), shown as mean ± S.D. with n = 12 biologically independent samples across two independent experiments, unless otherwise specified. **d,** Cell count of *M. tuberculosis* H37Ra infected murine macrophages (RAW 264.7) treated with increasing concentrations of MAD1 for 24 hours (black bars; n = 6 across two independent experiments). Macrophage viability at equivalent MAD1 concentrations shown as grey bars (n = 12 biologically independent samples across two independent experiments). Data presented as mean ± S.E.M. Statistical significance determined using a one-tailed Student's t-test relative to untreated control, with p values reported. **e,** Combinatorial synergy of MAD1 with first-line TB antibiotics isoniazid (INH), ethambutol (EMB) and rifampicin (RIF), as well as the second line anti-tubercular drug moxifloxacin (MOX). Fractional inhibition concentration (FIC) <1 and <0.5 are considered additive and synergistic, respectively. Data is presented as the FIC contribution of MAD1 against the contribution from the small molecule antibiotic.

Table 1 |

Minimum inhibitory concentration (MIC) of antitubercular peptides.

Species	Strain[a]	MIC (μM)[b]			
		MAD1 L(D)[c]	AMP1	AMP2	AMP3
Mycobacteria					
M. tuberculosis	H37Ra *(attenuated)*	2.5 (2.5)	20	10	20
M. tuberculosis	H37Rv *(virulent)*	5	-	-	-
M. bovis	TMC 1012	5(5)	10	20	10
M. bovis (INH-R)	TMC1103	5(5)	10	10	20
M. smegmatis	Mc^2 155	5(5)	20	20	20
Gram-positive					
S. aureus (MR)[d]	USA300*	>80 (20)	>80	80	20
S. aureus (MS)[d]	NRS72*	>80 (20)	>80	80	20
S. aureus (MS)[d]	Newman*	50 (>80)	80	40	20
B. anthracis	34F2 (Sterne)	>80 (5)	10	80	20
S. mitis	NCTC 12261*	>80 (10)	20	>80	40
E. faecalis	ATCC 29212	>80 (10)	80	>80	80
Gram-negative					
K. pneumoniae	NCTC 9633*	>80 (10)	20	20	2.5
E. coli	DH5α	40 (10)	>80	80	>80
S. enterica	CDC 6516–60	80 (10)	40	80	80
P. aeruginosa	PAO1*	50 (10)	10	20	80
A. baumannii	2208*	50 (5)	25	80	10
H. influenzae	TD-4*	80 (20)	80	80	40
Respiratory Selectivity Index[e]		**20**	**<1**	**2**	**<1**

[a] Lung commensals and pathobionts marked by a star

[b] Peptide sequences (prepared with amidated C-terminus): MAD1 - KRWHWWRRHWVVW-NH_2, AMP1 - WKWLKKWIK-NH_2, AMP2 - KRWWKWWRR-NH_2, AMP3 - RRWWRWVVW-NH_2

[c] L-peptide (D - chiral enantiomer)

[d] MR = Methicillin-resistant, MS = Methicillin-sensitive

[e] Respiratory selectivity index was determined relative to lung commensals and pathobionts, calculated as the lowest $MIC_{insensitive\ respiratory\ microbe}$ divided by $MIC_{Mtb\text{-}H37Ra}$.